https://dx.doi.org/10.1016/j.ultras.2023.107144

Modelling Guided Waves in Acoustoelastic and Complex Waveguides: from SAFE Theory to an Open-source Tool

Menglong LIU[a*], Wenyan ZHANG[a], Xiao CHEN[a], Lun LI[a], Kai WANG[b,c], Hong Wang[d], Fangsen CUI[e], Zhongqing SU[f]

[a] School of Mechanical Engineering and Automation, Harbin Institute of Technology, Shenzhen 518055, P.R. China

[b] School of Aerospace, Xiamen University, Xiamen 361102, P.R. China

[c] Innovation Laboratory for Sciences and Technologies of Energy Materials of Fujian Province (IKKEM), Xiamen 361005, P. R. China

[d] School of Management, Shenzhen University, Shenzhen 518060, P. R. China

e Institute of High Performance Computing, Agency for Science, Technology and Research, Singapore 138632, Singapore

[f] Department of Mechanical Engineering, The Hong Kong Polytechnic University, Kowloon, Hong Kong, P.R. China

Revised and Resubmitted to *Ultrasonics*

[*] To whom correspondence should be addressed. Email: liumenglong@hit.edu.cn. (Assistant Prof. Menglong LIU, *Ph.D.*)

Abstract. Guided waves (GW)-based techniques have been extensively investigated and applied in material characterization, damage detection, and structural health monitoring. A comprehensive understanding of GW is the cornerstone for the development of such techniques. Based on the semi-analytical finite element (SAFE) method, an open-source dispersion calculator of GW propagating in acoustoelastic and complex waveguides with both isotropic and anisotropic material properties is developed. First, by assuming the simple harmonic motion along the propagation direction and discretizing along the thickness direction, 1D-GLL-SAFE (one-dimensional Gauss-Lobatto-Legendre SAFE) is adopted for the solution of GW in plate waveguide, which is attributed to its superior performance in terms of computational accuracy and efficiency. Different theories on acoustoelasticity are adopted to calculate GWs under loading. Then 2D-Gauss-SAFE (two-dimensional Gauss SAFE) with triangular meshes filling the cross section is adopted for GW in general waveguides considering the ease of convenience in meshing. Finally, based on the 1D-GLL-SAFE and 2D-Gauss-SAFE algorithms, an open-source tool SAFEDC (SAFE-based dispersion calculator) is developed, which not only provides the solution of GW in pre-stressed isotropic waveguide and general cross section, but also extends to GW in laminates with arbitrary layer stacking configurations and hybrid stacking including multiple materials. Most of the GW features, including phase velocity, group velocity, wave number, wave structure in terms of displacement, stress, and strain, and animation of wave propagation are all offered in SAFEDC, which helps the researchers and engineers to understand and utilize GW.

Keywords: guided wave; semi-analytical finite element; dispersion curve; acoustoelasticity

1. Introduction

Guided waves (GWs) have been intensively studied for research and applications in material characterization, damage detection, and structural health monitoring (SHM)[1,2]. Significantly different from the bulk waves which usually have a limited number of modes with constant velocities over a wide frequency range, GWs are characterized by the frequency dispersion and multiple-modes, such that each GW mode at different frequencies may have different phase velocity, group velocity, and mode shape, providing rich information for various researches and applications. For example, the characterization of both elastic and viscoelastic material parameters has been realized with numerous machine learning and

parameter optimization algorithms [3,4], where GWs of multiple modes and frequencies along different directions need to be obtained. For the rapid detection of corrosion and cracks in pipelines, GW-based techniques have been commercialized by several companies: Guided Wave NDT by Applus+[5], SONYKS guided wave testing by Eddyfi[6], and subsea solutions by GUL[7], to name a few. The torsional wave T(0,1) at low frequency is generally the most preferred mode due to its non-dispersion and low demands on the transduction system. In addition, enabled by the miniaturized transducers that can be integrated into the monitored structure, GW-based SHM in an *in situ* and online way has seen a burgeoning development [8–12], such as the monitoring of corrosion, disbonding, delamination, crack, bolt looseness, and residual stress. In contrast, the bulk-wave based techniques, which are limited in coverage area, are generally combined with scanning equipment [13,14], and are therefore more suitable for off-line defect detection.

Understanding how GWs propagate along the waveguide of interest serves as the cornerstone for various GW-based techniques. Starting from a century ago when the governing equation of Lamb wave in the stress-free isotropic plate was derived [15], a number of analytical methods have been proposed to obtain the dispersion characteristics of GW in various waveguides, such as partial wave technique, global matrix method, transfer matrix method [16]. Afterwards, the influence of stress on GW in the plate waveguide is intensively investigated based on the governing equations with the theory of acoustoelasticity (TAE) included [17–19]. However, there are still some different approaches on the TAE to compute GWs. The governing equation of wave motion in the stressed waveguide in the natural, or undeformed, coordinate systems is adopted frequently [17,18,20,21], which, as claimed in Ref. [19], may result in the loss of both the constitutive and the geometric nonlinearities in the initial, or deformed, state. In addition, although the direct expression of effective elastic constant (EEC) enables the computation of GW under loading easily via the input of an equivalent anisotropic material into some off-the-shelf tools such as Disperse [22], the splitting of EECs make the solution not unique [23].

On the other hand, to deal with waveguides with general cross section, it is usually difficult to find the analytical equations, so techniques involving numerical methods have been developed, such as the semi-analytical finite element method (SAFE) [24,25] or semi-analytical isogeometric analysis (SAIGA) [26].

By discretizing the waveguide cross section with elements and assuming a simple harmonic motion along the propagation direction, SAFE and SAIGA are able to calculate the GW in waveguides from plate to general section, e.g. rectangular bar subjected to hydrostatic pressure [21], rail track subjected to both thermal and stress loading [20].

As concluded above, although the computation of GW propagation characteristics can be performed by individual researchers via coding or commercial software such as the PDE module in COMSOL[21], it is a daunting task to correctly obtain various characteristics of GW along the investigated waveguides, especially when the waveguide cross section or laminate layer stacking configuration is complex. Therefore, based on the above algorithms, several off-the-shelf tools have been developed that are capable of computing GW dispersion characteristics. The well-known tool Disperse [22], developed at Imperial College, focuses mainly on plate structure and tube structures with uniform inner and outer radii. The newly developed tool Dispersion Calculator (DC) [27] at the German Aerospace Center also targets the plate structure, particularly for laminates with hundreds of layers. The latest version of DC includes the ability to calculate the GW along the plate immersed in the fluid. GUIGUW [28] has also been developed at the University of Bologna as a tool capable of calculating GWs both in the plate and in the general waveguide. Another tool called LAMSS-COMPOSITES [29], developed at the University of South Carolina, is able to display the dispersion curves and steering angles of GW in several common composite laminates from a database, but is not able to compute the GW with user-defined parameters or material properties.

From the review of the literature and off-the-shelf GW computation tools, it is concluded that GWs in various waveguides can be computed using SAFE. Nevertheless, the tedious and time-consuming solution of eigenvalues and eigenvectors especially for thick laminates and complex waveguides with irregular geometric shape may hinder the application of SAFE. Therefore, how to achieve a balance among computational accuracy, efficiency, and wide applicability to various waveguides with SAFE is still an urgent need. Previously, the authors have developed the GLL-SAFE algorithm, which features a non-uniform node collation and Lobatto quadrature to obtain a diagonal mass matrix, to successfully realize the computation of GWs in isotropic plates, anisotropic laminates, and general waveguides such as railway

tracks, and demonstrated the improvement of both accuracy and efficiency over the conventional Gauss-SAFE with uniform node collation and Gauss quadrature[30]. In the developed GLL-SAFE for waveguide with complex geometry, Abaqus/CAE was used to mesh the general waveguide with quadratic quadrilateral elements, which were then imported into the GLL-SAFE algorithm. However, the introduction of an additional CAE software to mesh the general waveguide is not convenient in practice, and is therefore not a preferred choice for the development of tools to compute GW in general waveguides.

To address the above bottlenecks, this study proposes to combine 1D-GLL-SAFE with 1D elements to compute GWs in plate structures, and 2D-Gauss-SAFE with 2D quadratic triangular elements to compute GWs in waveguides with acoustoelasticity and complex geometry shape. Two governing equations based on the natural and initial coordinate systems, respectively, are intensively investigated to obtain velocities of GWs for quantitative comparison. The combined algorithms enable the interrogation of GWs in general waveguides of acoustoelasticity with a comprehensive consideration of computational accuracy, efficiency, and applicability. In addition, in order to make the GW functions available to both researchers and engineers, an open-source tool called SAFEDC (SAFE-based dispersion calculator) has been developed for GW computation using the MATLAB App Designer due to its convenience combined with high efficiency of matrix manipulation and numerical computation. SAFEDC provides comprehensive GW characteristics, including phase velocity, group velocity, wave number, wave structure in terms of displacement, stress, and strain, and wave propagation animation.

The rest of the paper is organized as follows. Section 2 briefs the derivation of SAFE with acoustoelasticity based on two different governing equations. Section 3 introduces the development of SAFEDC, followed by the computation of GWs in various waveguides and acoustoelasticity in Section 4 and concluding remarks drawn in Section 5.

2. Analytical Derivation of 1D-GLL-SAFE and 2D-Gauss-SAFE

2.1 1D-GLL-SAFE

1D-GLL-SAFE focuses on the solution of GW in isotropic and anisotropic plates and laminates, as shown in Figure 1a and b, respectively. Considering the element in the 1D-GLL-SAFE with natural

coordinate $\xi \in [-1,1]$, the Lobatto polynomial $Lo_n(\xi)$ is expressed as the derivative of the Legendre polynomial $P_{n+1}(\xi)$ as

$$Lo_n(\xi) = P'_{n+1}(\xi) = \frac{1}{2^{n+1}(n+1)!}\frac{d^{n+2}}{d\xi^{n+2}}[(\xi^2-1)^{n+1}]. \quad (1)$$

With polynomial order p, $Lo_p(\xi) = 0$ gives the zero points $\xi_0^{Lo_{p-1}}$, which, added to two end points -1 and 1, form the GLL-based nodes in the direction ξ expressed as:

$$\xi_i = \left\{-1, \xi_0^{Lo_{p-1}}, 1\right\}. \quad (2)$$

Thus, 1D-GLL-SAFE has a non-uniform distribution of nodes in the element, as shown in Figure 1a with $p_\xi = 3$. In the special case with $p_\xi = 2$ as shown in Figure 1b, the only internal node happens to be uniformly distributed at $\xi = 0$.

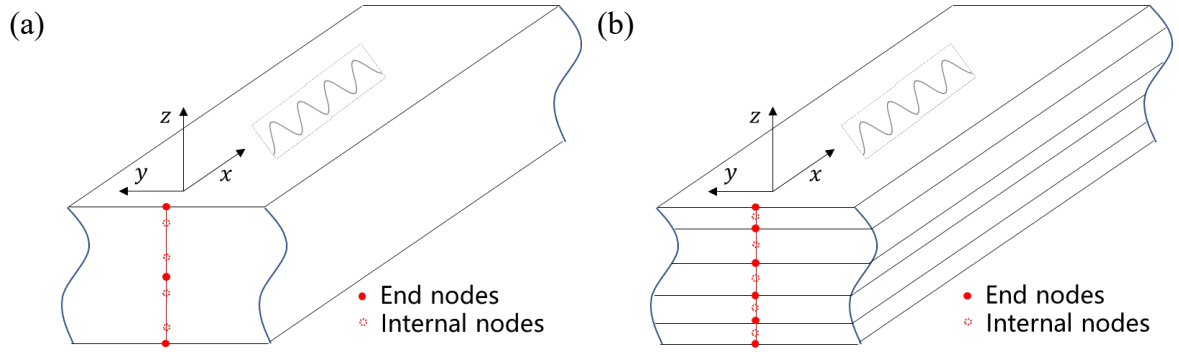

Figure 1 Illustration of 1D-GLL-SAFE (a) in the lamina with $p_\xi = 3$ and two elements, and (b) in the five-layer laminate with $p_\xi = 2$ and one element per layer

In 1D-GLL-SAFE, the particle displacement vector $\mathbf{u}^{(e)}$ is typically expressed in terms of shape functions and node displacements as:

$$\mathbf{u}^{(e)} = \left[u_x^{(e)} \quad u_y^{(e)} \quad u_z^{(e)}\right]^T = \mathbf{N}(\xi)\mathbf{Q}^{(e)}e^{i(kx-\omega t)}, \quad (3)$$

where $\mathbf{N}(\xi)$ is the interpolation shape function of element along the thickness direction, $\mathbf{Q}^{(e)}$ is the nodal displacement vector of the element, k is the wave number along the wave vector direction x, ω denotes the angular frequency, and t is time.

A governing equation for the wave motion within each element can be obtained through the virtual work principle as:

$$\int_{\Gamma} \delta \mathbf{u}^{(e)\mathrm{T}} \mathbf{t}^{(e)} d\Gamma = \int_{V} \delta \mathbf{u}^{(e)\mathrm{T}} (\rho^{(e)} \ddot{\mathbf{u}}^{(e)}) dV + \int_{V} \delta \boldsymbol{\varepsilon}^{(e)\mathrm{T}} \boldsymbol{\sigma}^{(e)} dV \tag{4}$$

where $\delta \mathbf{u}^{(e)}$ and $\delta \boldsymbol{\varepsilon}^{(e)}$ are the virtual displacement and virtual strain, respectively, $\mathbf{t}^{(e)}$ and $\boldsymbol{\sigma}^{(e)}$ denotes the external traction vector and stress vector, respectively, $\bullet^{T}$ denotes a complex conjugate transpose, $\rho^{(e)}$ is density, $\ddot{\bullet}$ is a second derivative with respect to time, Γ is the element surface, and V is the element volume.

Note that at the unstressed status, $\mathbf{C}$ is the material stiffness matrix which governs the relation of stress and strain vectors,

$$\boldsymbol{\sigma}^{(e)} = \mathbf{C} \boldsymbol{\varepsilon}^{(e)}. \tag{5}$$

the strain vectors at any point can be expressed as:

$$\boldsymbol{\varepsilon}^{(e)} = \left[\mathbf{L}_x \frac{\partial}{\partial x} + \mathbf{L}_y \frac{\partial}{\partial y} + \mathbf{L}_z \frac{\partial}{\partial z} \right] \mathbf{u}^{(e)}, \tag{6}$$

where

$$\mathbf{L}_x = \begin{bmatrix} 1 & 0 & 0 \\ 0 & 0 & 0 \\ 0 & 0 & 0 \\ 0 & 0 & 0 \\ 0 & 0 & 1 \\ 0 & 1 & 0 \end{bmatrix}, \mathbf{L}_y = \begin{bmatrix} 0 & 0 & 0 \\ 0 & 1 & 0 \\ 0 & 0 & 0 \\ 0 & 0 & 1 \\ 0 & 0 & 0 \\ 1 & 0 & 0 \end{bmatrix}, \mathbf{L}_z = \begin{bmatrix} 0 & 0 & 0 \\ 0 & 0 & 0 \\ 0 & 0 & 1 \\ 0 & 1 & 0 \\ 1 & 0 & 0 \\ 0 & 0 & 0 \end{bmatrix}, \tag{7}$$

where the second term in the right hand of Eq. (6) can be ignored for the 1D element, which is retained for the following 2D element in Section 2.2.

Substituting Eq. (3) into Eq. (6), the expression of the strain vector is simplified as:

$$\boldsymbol{\varepsilon}^{(e)} = \left(\mathbf{B}_1 + ik\mathbf{B}_2 \right) \mathbf{Q}^{(e)} e^{i(kx - \omega t)}, \tag{8}$$

where $\mathbf{B}_1 = \mathbf{L}_y \mathbf{N}_{,y} + \mathbf{L}_z \mathbf{N}_{,z}$ and $\mathbf{B}_2 = \mathbf{L}_x \mathbf{N}$.

Then substituting Eq. (5) and Eq. (8) into Eq.(4), assembling all the elements, and applying the traction-free boundary conditions, the eigenvalue equation of the entire system can be obtained as:

$$(\mathbf{K}_1 + ik\mathbf{K}_2 + k^2 \mathbf{K}_3 - \omega^2 \mathbf{M}) \mathbf{Q} = \mathbf{0}, \tag{9}$$

where the global stiffness matrix $\mathbf{K}_1, \mathbf{K}_2, \mathbf{K}_3$, and the global mass matrix $\mathbf{M}$ are assembled from individual element stiffness matrix $\mathbf{K}_1^{(e)}, \mathbf{K}_2^{(e)}, \mathbf{K}_3^{(e)}$ and element mass matrix $\mathbf{M}^{(e)}$, which are expressed as:

$$\begin{cases} \mathbf{K}_1^{(e)} = \int_{-1}^{1} \mathbf{B}_1^T \mathbf{C} \mathbf{B}_1 d\xi \\ \mathbf{K}_2^{(e)} = \int_{-1}^{1} (\mathbf{B}_1^T \mathbf{C} \mathbf{B}_2 - \mathbf{B}_2^T \mathbf{C} \mathbf{B}_1) d\xi \\ \mathbf{K}_3^{(e)} = \int_{-1}^{1} \mathbf{B}_2^T \mathbf{C} \mathbf{B}_2 d\xi \\ \mathbf{M}^{(e)} = \int_{-1}^{1} \rho^{(e)} \mathbf{N}^T \mathbf{N} d\xi \end{cases}. \tag{10}$$

The size of the matrices $\mathbf{K_1}$, $\mathbf{K_2}$, $\mathbf{K_3}$ and $\mathbf{M}$ is $3N \times 3N$, where N is the total number of nodes. $\mathbf{Q}$ is a $3N \times 1$ vector representing the node displacements. $\mathbf{C}$, with size of 6×6, is the material stiffness matrix which governs the relation of stress and strain vectors. In 1D-GLL-SAFE, the Lobatto quadrature is used to calculate the mass matrix, which is derived to be diagonal. This not only greatly improves the efficiency of the matrix inversion, but also reduces the induced computational error.

Two approaches are commonly used to solve Eq. (9). The first approach is that for a fixed wave number k, the angular frequency ω is computed by treating ω^2 as an unknown eigenvalue. For a fixed k, multiple values of ω are obtained, each denoting the angular frequency of a mode. The solved eigenvector $\mathbf{Q}$ at each ω is the corresponding displacement mode shape. The second approach is that, given a fixed angular frequency ω, the wave number k can also be computed, but the size of the matrix for solving the eigenvalues and eigenvectors is doubled to $6N \times 6N$, which will significantly increase the computation time. Therefore, to improve the computational efficiency, the first approach is adopted in this study, and the second approach must be adopted when considering the wave attenuation with the wave number with non-zero imaginary part, which includes propagating GWs in the waveguide composed of viscoelastic material or immersed in liquid/solid, and evanescent GWs in the waveguide with elastic material.

After solving Eq. (9), the computed eigenvalues with only real part denote the propagating GW modes.

To facilitate the understanding of the dispersion characteristics of each mode, these eigenvalue points in the specified wave number range are sorted into different wave modes using the orthogonality-based wave mode sorting algorithm [31]. It is assumed that the orthogonality relation approximately holds for eigenvectors solved at two neighboring wave numbers k and $k+\Delta k$:

$$\begin{cases} \mathbf{Q}_m^T(k)\mathbf{M}_m(k)\mathbf{Q}_m(k+\Delta k) \neq 0 \\ \mathbf{Q}_n^T(k)\mathbf{M}_m(k)\mathbf{Q}_m(k+\Delta k) \approx 0 \end{cases} \tag{11}$$

After extracting eigenvalues and their corresponding eigenvectors from Eq. (9) for two neighboring wave numbers, orthogonality relations are computed between one eigenvector from the solutions with k and every eigenvector from the wave number solutions with $k+\Delta k$, yielding a vector of orthogonality values. Thus, Eq. (11) guarantees that if the two eigenvectors used in the orthogonality computation belong to the same wave mode, the maximum value of the vector will be obtained, indicating the mode match of the two eigenvectors. Then, the wave number solution is used to derive both the phase and the group velocity, which provides important information about the wave propagation. The derivation of group velocity is given in Appendix B. The corresponding eigenvector shows the mode shape of displacement, which can be used to derive the mode shape of stress and strain.

2.2 **2D-Gauss-SAFE**

2D-Gauss-SAFE is adopted to compute GWs in waveguides with complex geometry, such as the railway track with the cross section shown in Figure 2. Considering that triangular elements have better geometric adaptability to mesh complex geometry than quadrilateral elements, the GLL non-uniform node distribution adopted in the plate structutre is not extended to the 2D-SAFE with quandrilateral elements, and instead the quadratic 6-node triangular elements are used to discretize the cross section, and Gauss quadrature is adopted to compute the mass and stiffness matrix.

In 2D-Gauss-SAFE, the particle displacement vector $\mathbf{u}^{(e)}$ is expressed in terms of the shape functions and the node displacements as:

$$\mathbf{u}^{(e)} = \begin{bmatrix} u_x^{(e)} & u_y^{(e)} & u_z^{(e)} \end{bmatrix}^T = \mathbf{N}(\xi,\eta)\mathbf{Q}^{(e)} e^{i(kx-\omega t)}, \tag{12}$$

where ξ and η are the natural coordinates of the triangular element, and $\mathbf{N}(\xi,\eta)$ is the interpolation shape function matrix of element in the waveguide cross section, which is expressed based on

$$\begin{cases} N_1 = \xi(2\xi - 1) \ , \ N_4 = 4\xi\eta \\ N_2 = \eta(2\eta - 1) \ , \ N_5 = 4\zeta\eta \\ N_3 = \zeta(2\zeta - 1) \ , \ N_6 = 4\xi\zeta \end{cases}, \tag{13}$$

where $\zeta = 1 - \xi - \eta$.

Substituting Eq. (12) into the governing equation of Eq. (4) obtained by the virtual work principle, and after a series of derivations, the eigenvalue equation with the same form as Eq. (9) can be obtained for the quadratic triangular elements.

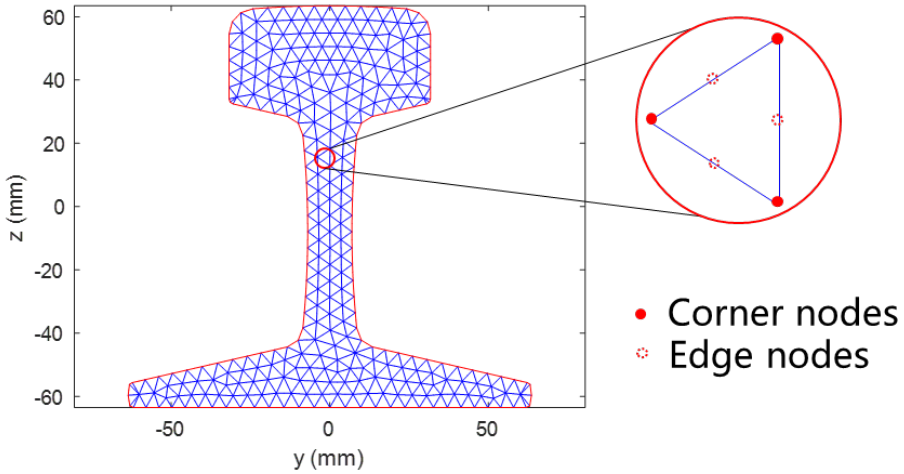

Figure 2 Illustrated mesh discretization of a railway track cross section

2.3 SAFE with Acoustoelasticity

Two governing equations of GW with acoustoelasticity based on the both the natural and initial coordinate systems are briefed as follows.

2.3.1 Governing Equation in the Natural Coordinate System

The GW with an acoustoelastic effect in an isotropic waveguide under stress is governed by the equation in the natural coordinate system with Eq. (85) in Ref. [23]:

$$\frac{\partial}{\partial \xi_\beta}\left[T_{\gamma\beta}^i \frac{\partial u_\alpha}{\partial \xi_\gamma} + \Gamma_{\alpha\beta\gamma\delta} \frac{\partial u_\gamma}{\partial \xi_\delta} \right] = \rho^0 \frac{\partial^2 u_\alpha}{\partial t^2}, \tag{14}$$

where $T_{\gamma\beta}^i$ and $\Gamma_{\alpha\beta\gamma\delta}$ are two coefficients combining the 2nd and 3rd order elastic constants and Lagrangian and Cauchy strains, which are expressed as

$$\begin{cases} T^i_{\gamma\beta} = C_{\gamma\beta\alpha\delta}E^i_{\alpha\delta} + \dfrac{1}{2}C_{\gamma\beta\alpha\delta\varepsilon\eta}E^i_{\alpha\delta}E^i_{\varepsilon\eta} \\ \Gamma_{\alpha\beta\gamma\delta} = C_{\alpha\beta\gamma\delta} + C_{\alpha\beta\lambda\delta}\dfrac{\partial u^i_\gamma}{\partial \xi_\lambda} + C_{\lambda\beta\gamma\delta}\dfrac{\partial u^i_\alpha}{\partial \xi_\lambda} + C_{\alpha\beta\gamma\delta\varepsilon\eta}e^i_{\varepsilon\eta} \end{cases}, \tag{15}$$

where the coordinates of a material point in the natural state is represented by the position vectors $\boldsymbol{\xi}$. The deformation from the natural to the initial states is static and the displacement of the particles is denoted by $\mathbf{u}^{\mathbf{i}}$, where the superscript "i" denotes the initial state under the static loading. $E^i_{\alpha\delta}$ and $e^i_{\varepsilon\eta}$ denote the Lagrangian strain tensor and infinitesimal (or Cauchy) strain tensors in the initial state under loading. C_{ijkl} is the quadratic elastic constant, which for isotropic materials is given by

$$C_{ijkl} = \lambda\delta_{ij} + \mu\left(\delta_{ik}\delta_{jl} + \delta_{il}\delta_{jk}\right), \tag{16}$$

where λ and μ are Lame constants and δ is the Kronecker delta function. The tensor C_{ijklmn} for isotropic materials can be expressed in terms of the Murnaghan constants l, m and n as

$$\begin{aligned} C_{ijklmn} = {} & 2\left(l - m + \frac{n}{2}\right)\delta_{ij}\delta_{kl}\delta_{mn} + 2\left(m - \frac{n}{2}\right)\left(\delta_{ij}I_{klmn} + \delta_{kl}I_{mnij} + \delta_{mn}I_{ijkl}\right) \\ & + \frac{n}{2}\left(\delta_{ik}I_{jlmn} + \delta_{il}I_{jkmn} + \delta_{jk}I_{ilmn} + \delta_{jl}I_{ikmn}\right) \end{aligned}, \tag{17}$$

where

$$I_{ijkl} = \frac{\left(\delta_{ik}\delta_{jl} + \delta_{il}\delta_{jk}\right)}{2}. \tag{18}$$

Substituting Eq. (15) into Eq. (14) gives

$$\frac{\partial}{\partial \xi_\beta}\left(\tilde{C}_{\alpha\beta\gamma\delta}\frac{\partial u_\gamma}{\partial \xi_\delta}\right) = \rho^0\frac{\partial^2 u_\alpha}{\partial t^2}, \tag{19}$$

where the effective elastic constant (EEC) $\tilde{C}_{\alpha\beta\gamma\delta}$ is expressed as

$$\tilde{C}_{\alpha\beta\gamma\delta} = C_{\alpha\beta\gamma\delta} + C_{\alpha\beta\lambda\delta}e^i_{\gamma\lambda} + C_{\alpha\beta\gamma\delta\varepsilon\eta}e^i_{\varepsilon\eta} + C_{\lambda\beta\gamma\delta}e^i_{\alpha\lambda} + C_{\beta\delta\varepsilon\eta}e^i_{\varepsilon\eta}\delta_{\alpha\gamma}. \tag{20}$$

$\tilde{C}_{\alpha\beta\gamma\delta}$ depicts the relationship between perturbed stress and strain due to GW propagating in a stressed isotropic waveguide. By replacing $\mathbf{C}$ in Eq. (10) with $\tilde{C}_{\alpha\beta\gamma\delta}$ in Eq. (20), the GW propagating in the stressed waveguide can be computed with SAFE. Note that in the special case that $e^i = 0$, $\tilde{C}_{\alpha\beta\gamma\delta}$ returns

to $C_{\alpha\beta\gamma\delta}$, which is used to compute the GW in the unstressed condition.

As reported in Ref. [23], to make use of the off-the-shelf tool Disperse, the fourth tensor $\tilde{C}_{\alpha\beta\gamma\delta}$ needs to be converted to a matrix with size of 6 × 6 using Voight notation, which leads to the splitting of the EEC for the stressed isotropic material. Thus, there will be two sets of calculated values corresponding to the two sets of EECs, each of which can be directly input into Eq. (10) for the solution of GWs with acoustoelasticity.

To avoid this splitting and to apply SAFE in the presence of stress, the following notation is used (11 → 1; 22 → 2; 33 → 3; 23 → 4; 31 → 5; 12 → 6; 32 → 7; 13 → 8; 21 → 9), allowing the rewriting of $\tilde{C}_{\alpha\beta\gamma\delta}$ as a 9 × 9 matrix. Applying the same notation to the gradient of displacement leads to the change of Eq. (7) into

$$\mathbf{L}_x=\begin{bmatrix}1&0&0\\0&0&0\\0&0&0\\0&0&0\\0&0&1\\0&0&0\\0&0&0\\0&0&0\\0&1&0\end{bmatrix},\mathbf{L}_y=\begin{bmatrix}0&0&0\\0&1&0\\0&0&0\\0&0&1\\0&0&0\\0&0&0\\0&0&0\\0&0&0\\1&0&0\end{bmatrix},\mathbf{L}_z=\begin{bmatrix}0&0&0\\0&0&0\\0&0&1\\0&1&0\\0&0&0\\0&0&0\\0&0&0\\1&0&0\\0&0&0\end{bmatrix} \tag{21}$$

With the retained 9 × 9 matrix of $\tilde{C}_{\alpha\beta\gamma\delta}$ and the accordingly adjusted gradient of displacement in Eq. (21), the GWs with acoustoelasticity can be calculated without the split EECs.

2.3.2 **Governing Equation in the Initial Coordinate System**

Another theoretical model in the initial coordinate system has been derived in Refs [19,32], in which the governing equation is expressed as

$$C_{abkl}^{eq}\frac{\partial^2 u_k^w}{\partial X_b \partial X_l}=\rho^0\frac{\partial^2 u_a^w}{\partial t^2}, \tag{22}$$

where u^w denotes the displacement describing the wave motion, and the coordinate of a material point in the initial state is represented by the position vectors $\mathbf{X}$, and the ECC is expressed as

$$C_{ijkl}^{eq} = C_{ijkl} + \sum_{q,r,m,n=1}^{3} \left(\left[\delta_{ik} C_{jlqr} \frac{\partial u_q^I}{\partial X_r} + C_{rjkl} \frac{\partial u_i^I}{\partial X_r} + C_{irkl} \frac{\partial u_j^I}{\partial X_r} + C_{ijrl} \frac{\partial u_k^I}{\partial X_r} + C_{ijkr} \frac{\partial u_l^I}{\partial X_r} \right] + \left[C_{ijklmn} \frac{\partial u_m^I}{\partial X_n} \right] \right). \quad (23)$$

The 4th tensor is kept throughout the entire derivation, and hence gradient of displacement is calculated based on Eq. (21), from which only one unique solution is obtained. All the details of the derivation can be found in Ref. [19].

3. Development of SAFEDC

Based on the developed 1D-GLL-SAFE and 2D-Gauss-SAFE algorithms, a graphical user interface-based open-source tool SAFEDC is developed, which requires no further coding to use. The SAFEDC framework is shown in Figure 3. The MATLAB App Designer is used to create a professional application that is easy to use and has high efficiency in matrix manipulation and numerical computation of MATLAB.

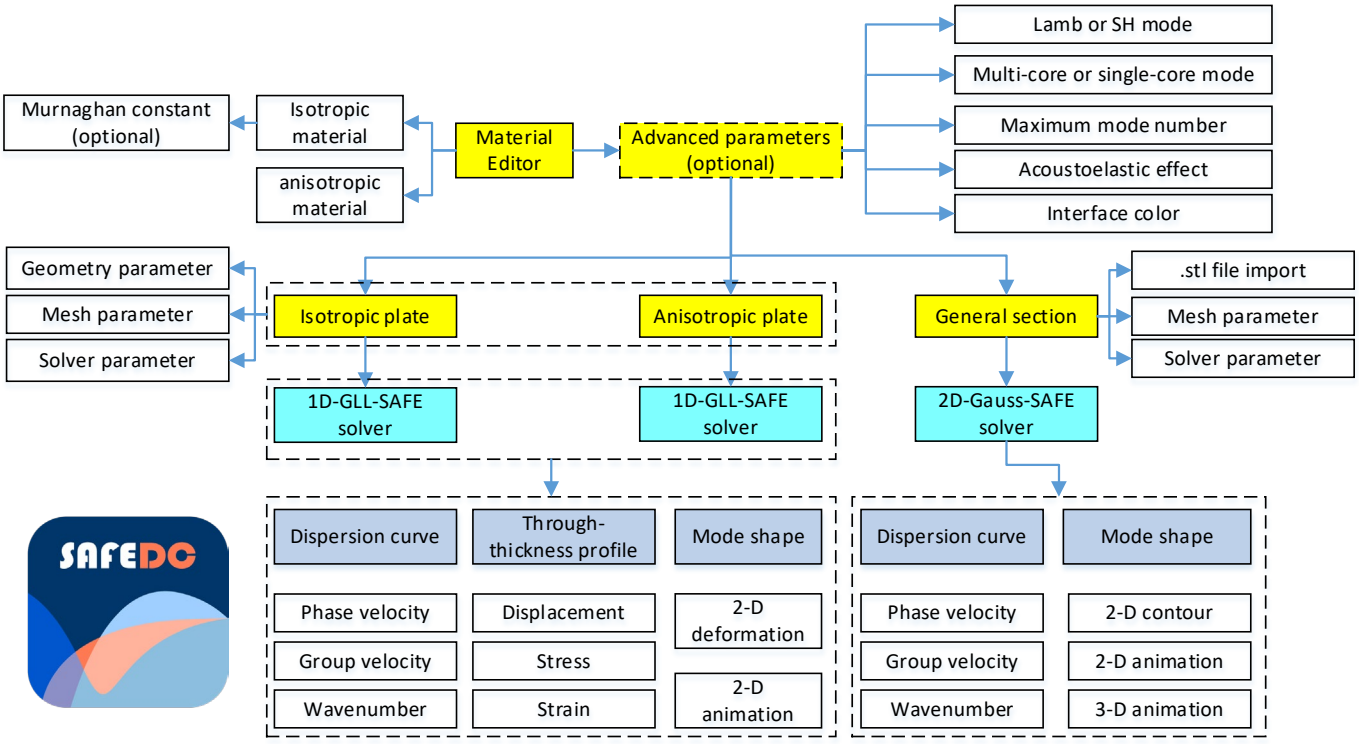

Figure 3 Framework of SAFEDC

In SAFEDC, five modules are designed and named as material editor, isotropic plate, anisotropic plate, general section, and advanced parameters, respectively. Each module is introduced as follows.

(1) Material editor. The default interface of the module “Material editor” is displayed in Figure A 1. Users need to enter the desired material property in the module of material editor, or simply select one of the common materials predefined in SAFEDC. Two categories of materials are included, namely isotropic

materials and anisotropic materials. For the latter, several classes of materials can be selected or defined, including orthotropic material, transversely isotropic material, and cubic symmetry material, and general anisotropic material, which contain 9, 5, 3, and 21 independent parameters, respectively. Note that three Murnaghan third order elastic constants are optional as the input of the isotropic material for the analysis of GW with acoustoelastic effect.

(2) Isotropic plate. A typical interface of the module "Isotropic plate" is displayed in Figure A 2. The module "Isotropic plate" focuses on computation of GW in an isotropic plate. At the end of the computation, dispersion curves in terms of phase velocity, group velocity, and wave number, through thickness profiles of displacement, stress, and strain, and 2D mode shape presented with static deformation and animation, can all be offered and saved. It is also worth noting that the computation of GW will take into account the acoustoelastic effect when the Murnaghan third order elastic constants are defined and the "Acoustoelastic effect" is enabled. Lamb wave and shear horizontal wave modes can be output separately by ticking the appropriate box in the module "Advanced parameters", and both modes are output by default. Note that two commonly used sets of Murnaghan third-order elastic moduli, either in the form of $l, m,$ and n or $A, B,$ and C, can be interconverted as follows[33]:

$$\begin{cases} n = A \\ m = B + A/2 \\ l = A + B + C \end{cases} \tag{24}$$

(3) Anisotropic plate. The default interface of the module "Anisotropic plate" is displayed in Figure A 3 and is basically the same as the that of "Isotropic plate". However, the geometric and material configurations of the anisotropic plate, as illustrated in Figure A 4, are performed separately, where the material name, angle, and thickness at each ply need to be specified, together with whether the stacking sequency is symmetric or not. In addition, by ticking the "Hybrid" box, it is possible to define different materials at each ply. After configuring the geometry and material, the following setups are basically the same as in the module "Isotropic plate", except that an additional parameter of propagation angle needs to be defined, as GW propagates differently along different propagation angles in an anisotropic lamina or laminate.

(4) General section. The module "General section" is very different from the module "Isotropic plate"

or “Anisotropic plate”. Common CAD software such as SOLIDWORKS and CATIA are used to create the STL file of a 2D surface representing the cross section of the waveguide. Note that although the STL describes the 3D geometry, the STL output of a single surface is available, and a constant coordinate in the 3rd dimension makes it an equivalent 2D model. As mentioned in Section 2, only quadratic triangular elements are used in 2D-Gauss-SAFE for both convenience and accuracy. After meshing with the desired sizes, and setting the material and computational parameters, the dispersion characteristics of the GW can be computed. Both isotropic and anisotropic materials are supported in SAFEDC, but for the latter, two direction vectors must be input to specify the material principal directions of x and y, to allow the rotation of anisotropic material. Note that the acoustoelastic effect along the propagation direction can also be included in the computation of the GW in the isotropic general section. After computation, dispersion curves and mode shapes of the GW are provided. As the waveguide has a 2D general section, the mode shape of the displacement will be presented with three 2D contours. In addition, both 2D and 3D animations of displacement for each mode are provided in SAFEDC to clearly demonstrate the propagation of the GW.

(5) Advanced parameters. The module “Advanced parameters” focuses on the setting of advanced parameters that are required by default. E.g., one of the functions “Interface color” is added to enable users to adjust the color theme. “Multicore computation” is enabled by default, but it is optional to disable the multicore computation in case that SAFEDC is running on a poorly performing computer where multicore computation may consume too much memory. For isotropic plates, the separation of Lamb modes and shear horizontal modes can be selected. The acoustoelasticity can also be enabled in this module.

4. Validation of GWs in Various Waveguides

To illustrate the developed algorithms 1D-GLL-SAFE and 2D-Gauss-SAFE, and the functionality of the software SAFEDC, GWs in three unstressed typical waveguides, i.e., aluminum plate, CFRP laminate, and rail track, and in a stressed aluminum plate, are investigated.

4.1 Isotropic plate - aluminum plate

The unstressed 4 mm thick isotropic aluminum 6061 plate is adopted for the first illustration of the GW computation in the isotropic plate, whose property is shown in Table 1. The computation was run via a desktop with the CPU AMD Ryzen 9 3950X 16-Core Processor and 32 Gigabytes RAM. With the element size set as 0.2 mm, 20 elements are generated for the computation, which takes 15.33 s and 3.70s

respectively for computation with single core and multiple cores. The most time consuming part of SAFEDC is the solution of eigenvalues and eigenvectors in Eq. (9), which takes more than half of the entire computation time.

Table 1. Material parameter of three unstressed waveguides.

Name	density	Stiffness property	Type
Al 6061	2700 kg/m^3	$E = 68$ GPa $\nu = 0.33$	isotropic
AS4M3502	1550 kg/m^3	$E_1 = 144.65$ GPa $E_2 = 9.64$ GPa $G_{12} = 6.00$ GPa $G_{23} = 3.75$ GPa $\nu_{12} = 0.299$	transversely isotropic
Steel 1020	7850 kg/m^3	$E = 207$ GPa $\nu = 0.3$	isotropic

Table 2. Computational information of three waveguides without loading.

Name	geometry	Element size	Element number	Time (single core)	Time (multiple cores)
Al 6061 plate	4 mm thick	0.2 mm	20	15.33 s	3.70 s
AS4M3502 laminate	[0/90/-45/45]2s 2 mm thick	0.0625 mm	32	109.05 s	23.32 s
Steel 1020 rail track	Imported externally	4 -6 mm	389	83.16 s	27.69 s

The dispersion curves of phase velocity, group velocity, and wave number with the frequency are computed with 1D-GLL-SAFE (see Figure 4a to c), and with the off-the-shelf tool DC (see Figure 4d to f). The relative errors between the two groups of results are calculated as

$$\delta = \frac{|v_1 - v_0|}{v_0}, \tag{25}$$

where v_1 is the velocity or wave number calculated with 1D-GLL-SAFE, v_0 is that calculated with DC. The calculated errors of phase velocity (see Figure 4g) and wave number (see Figure 4i) for the fundamental A0 and S0 modes all reach below 1×10^{-4}, while that of the group velocity (see Figure 4h) can also reach

below 1×10^{-2}, confirming the correctness of the developed algorithm.

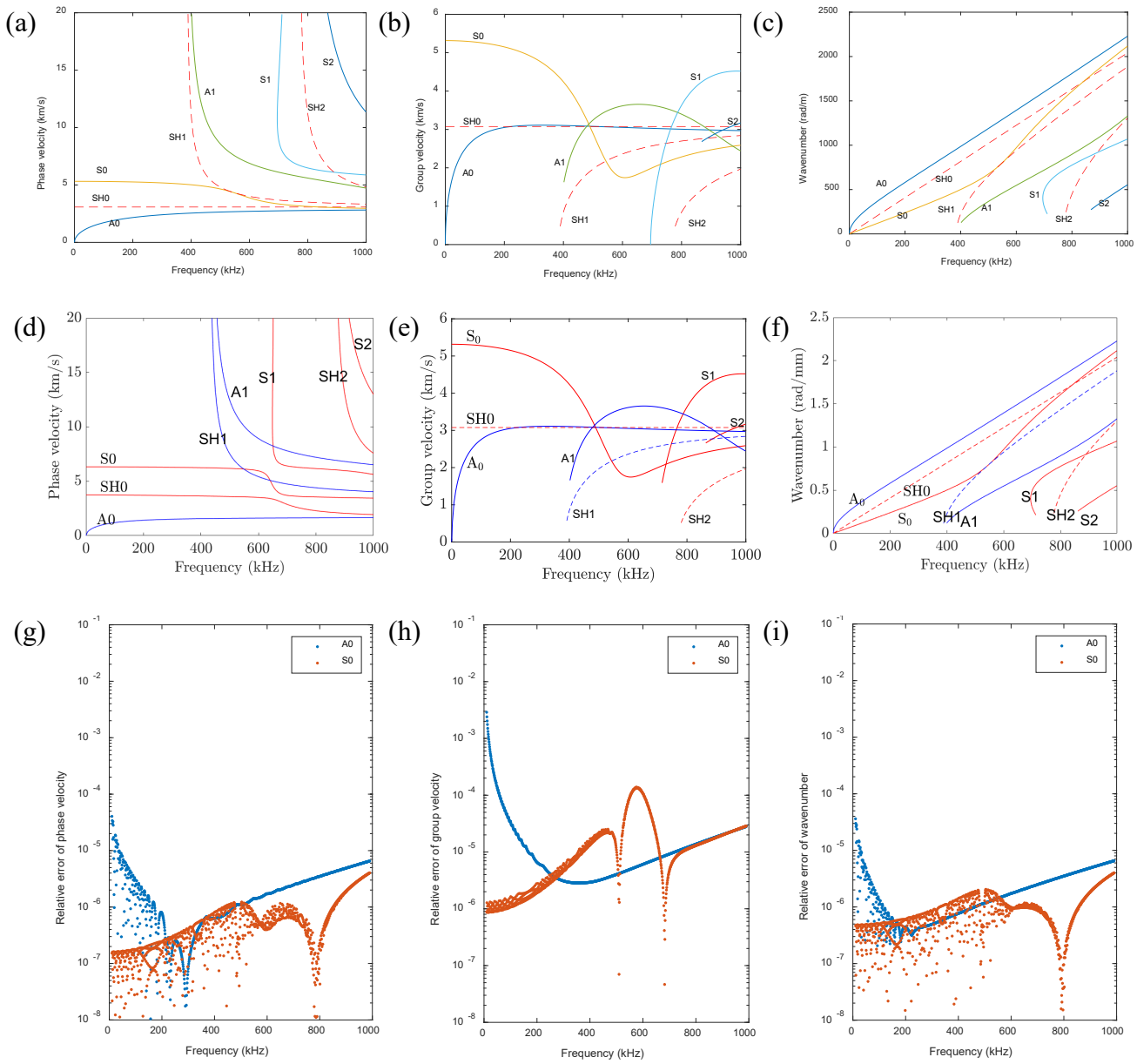

Figure 4 Dispersion curves of GW along a 4 mm thick aluminum plate: (a) phase velocity from SAFEDC, (b) group velocity from SAFEDC, (c) wave number from SAFEC, (d) phase velocity from DC, (e) group velocity from DC, (f) wave number from DC, (g) relative error of phase velocity, (h) relative error of group velocity, and (i) relative error of wave number.

The mode shapes of A0 and SH0 at ~1000 kHz are displayed in Figure 5. Note that for Mode A0, the mode shape is plotted along the propagation and thickness direction, while for Mode SH0, the mode shape is plotted along the in-plane transverse and thickness direction. Both mode shapes clearly display how different GWs propagate.

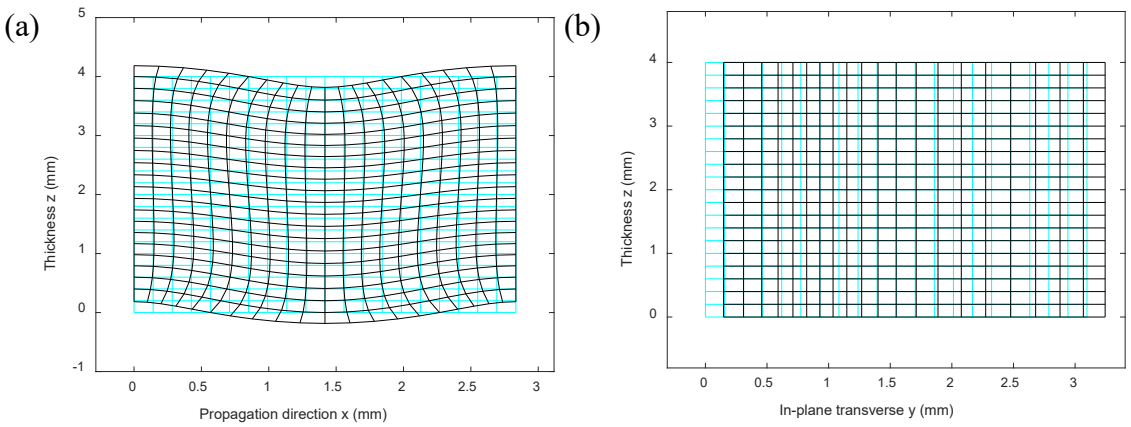

Figure 5 Mode shape of displacement superimposed with undistorted shape for GW along 4 mm thick aluminum plate at ~1000 kHz: (a) Mode A0, (b) Mode SH0

Also, the normalized through thickness profiles of displacement, stress, and strain are calculated with 1D-GLL-SAFE for all the computed modes at the computed frequency range. The normalization is performed based on the maximum value of all the components. The normalized displacements of Mode A0 and SH0 are shown in Figure 6, where there are non-zero in-plane and out-of-plane displacements for mode A0 and only non-zero in-plane transverse displacement for Mode SH0. The anti-symmetry of the Mode A0 and the shear horizontal Mode SH0 can be easily discerned with the through thickness profile of the displacement. For illustration, the normalized six stress and strain components of Mode A0 at ~1000 kHz are shown in Figure 7, in which three strain components ($\epsilon_{22}, \epsilon_{23},$ and ϵ_{12}) are zero, which agrees well with the assumption of plane strain for Lamb wave.

The displacement, stress, and strain profiles are of great significance to the selection of wave excitation and sensing techniques. For example, most 1D laser vibrometers measure the out-of-plane velocity or displacement, and bonded PZT wafers poled along the out-of-plane direction are most sensitive to in-plane stress and strain with the piezoelectric coefficient d_{31}. Similarly, when investigating the second harmonic wave with the S1-S2 mode pair, the in-plane loading must be transferred from the wedge to the specimen with the coupling gel as there is no out-of-plane displacement for the S1 mode at the matched frequency [34].

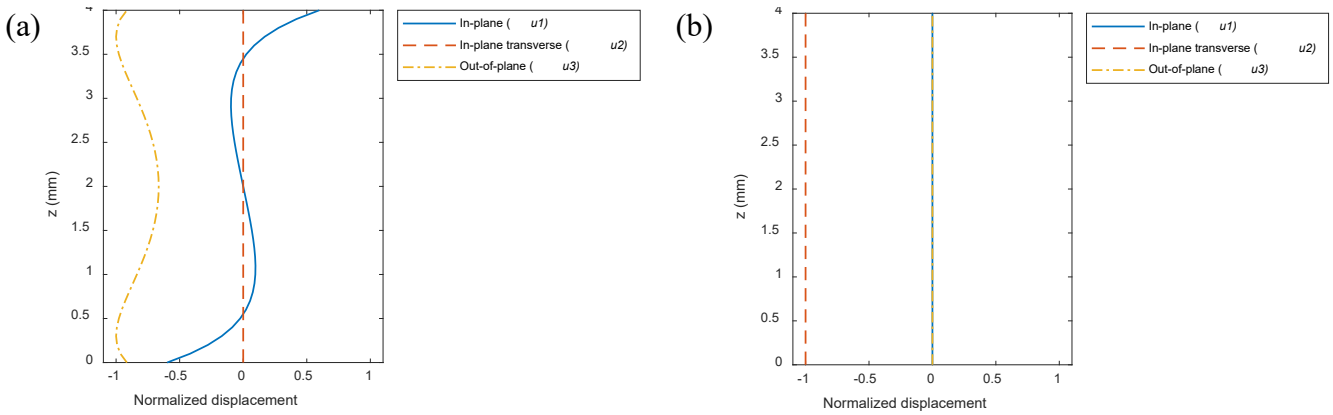

Figure 6 Through-thickness profile of displacement for GW propagating in a 4 mm thick aluminum plate at ~1000 kHz: (a) Mode A0, and (b) Mode SH0

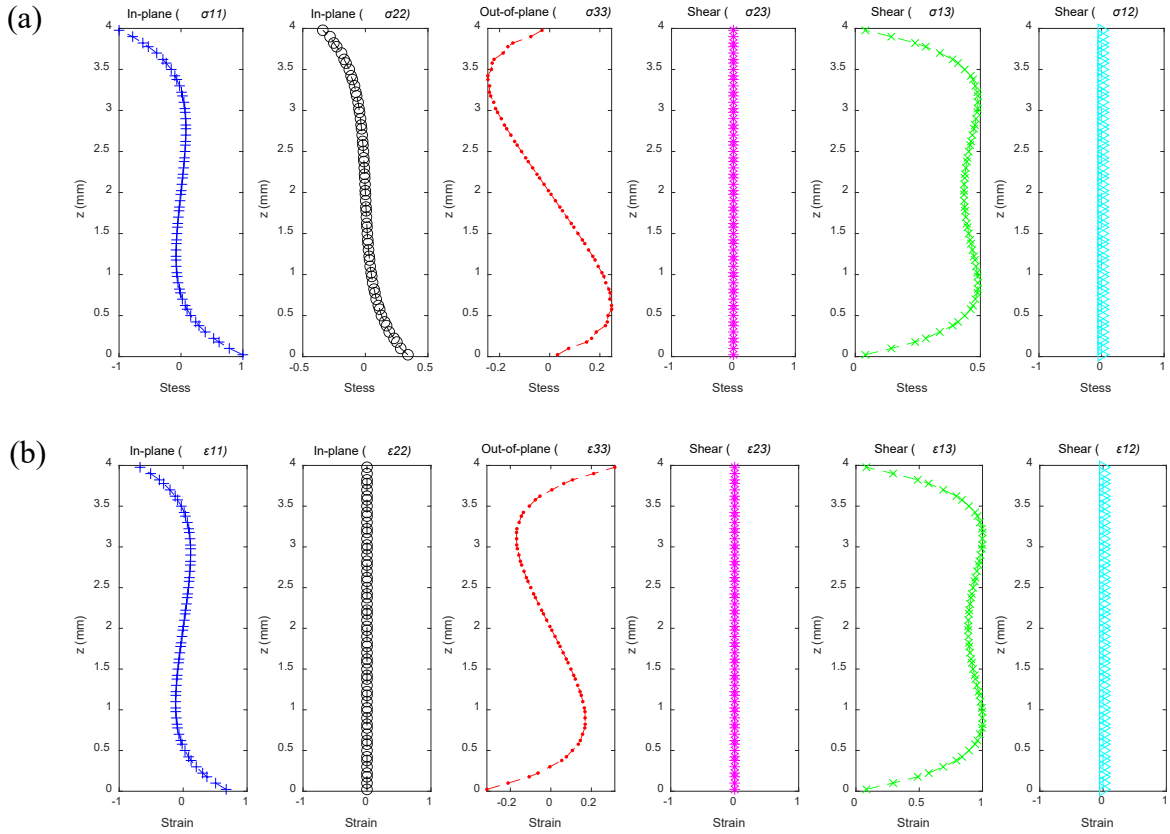

Figure 7 Through-thickness profile of Mode A0 at ~1000 kHz: (a) stress and (b) strain

4.2 **Stressed isotropic plate - aluminum plate**

The developed 1D-GLL-SAFE is also able to include the acoustoelastic effect in the computation of the GW. To quantitatively compare the calculated results based on Eq. (14) in the natural coordinate and Eq. (22) in the initial coordinate, the Lamé parameters are set as $\lambda = 56.35$ GPa and $\mu = 27.5$ GPa, the density $\rho = 2704\ \mathrm{kg/m^3}$, the thickness 6.35 mm, and Murnaghan constants $l = -281.5$ GPa, $m = -339$ GPa, and $n = -416$ GPa. The pre-stress is increased from 0 MPa to 60 MPa at an increment of 10 MPa, whose influence on the change of phase velocity is shown in Figure 8, with the legends explained in

1 Table 3.

2 Table 3. Explanation of legends in Figure 8.

legend	meaning
Abderahmane ini (Thickness)	Result at deformed initial coordinate based on Ref. [19] with stress-induced thickness variation considered
Gandhi ini (Thickness)	Result at deformed initial coordinate based on Ref. [17], with stress-induced thickness variation added
Abderahmane ini	Result at deformed initial coordinate based on Ref. [19] with stress-induced thickness variation not considered
Gandhi ini	Result at deformed initial coordinate based on Ref. [17], but with stress-induced thickness variation not considered
Gandhi ini ABBA	Result at deformed initial coordinate based on split ECC in Row 2 and 4 in Eq. (111) in Ref. [23], but with stress-induced thickness variation not considered
Gandhi ini ABAB	Result at deformed initial coordinate based on split ECC in Row 1 and 3 in Eq. (111) in Ref. [23], but with stress-induced thickness variation not added
Gandhi nat	Result at un-deformed natural coordinate based on Ref. [17], but with stress-induced thickness variation not considered
Gandhi nat ABBA	Result at un-deformed natural coordinate based on split ECC in Row 2 and 4 in Eq. (111) in Ref. [23], but with stress-induced thickness variation not added
Gandhi nat ABAB	Result at un-deformed natural coordinate based on split ECC in Row 1 and 3 in Eq. (111) in Ref. [23], but with stress-induced thickness variation not added

3

4 As shown in Figure 8, all the calculated results expressed with the legends “Abderahmane ini
5 (Thickness)” and “Gandhi ini (Thickness)” show highly matched values with a maximum difference of
6 phase velocity ~ 1 m/s at 40 MPa loading. This match also applies to the case with thickness variation not
7 considered or to the case in the natural coordinate. However, the splitting of ECCs leads to the increased
8 error to some degree, but still within an acceptable range of less than 2 m/s at 40 MPa loading.

9 The zoom-in of Figure 8 shows how the thickness variation under the loading influences the wave
10 velocity of three GWs at (250 kHz, S0), (400 kHz, A1), and (600 kHz, S1), in which only 0.1 m/s, 1.1 m/s,

and 0.5 m/s velocity change is obtained at 40 MPa loading. Another aspect to notice is that although it is claimed that the developed theory based on the initial coordinate in Ref. [19] achieves a higher accuracy than that in the calculated result in Ref. [17], the results in Ref. [19] calculate the change of the phase velocity after deformation, which is ignored for both the theoretical and experimental results in Ref. [17]. When this difference is compensated, both theories in Refs. [17,19] give similar results.

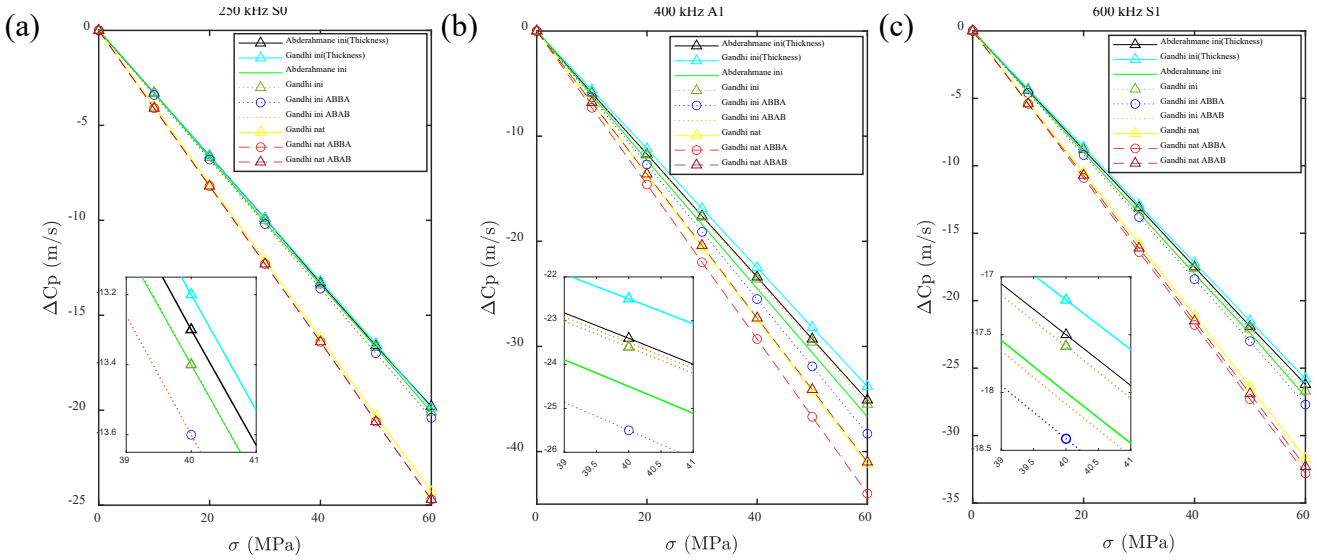

Figure 8 Comparison of various calculations including Abderahmane et al. Ref. [19], Gandhi et al., Refs. [17,23].

Calculated based on the governing equation in Eq. (22), the differences of phase and group velocity of modes A0, S0, and A1 after deformation at the unidirectional loading from 25 MPa to 100 MPa at an increment of 25 MPa from those without loading are displayed in Figure 9. Both the length and thickness variations are included. This situation corresponds to the measurement with a fixed distance between the excitation and acquisition. The different sensitivities of the three GW modes at different frequencies to stress provide an insight into the selection of appropriate GW to characterize stress values. E.g., as shown in Figure 9a, the phase velocity of Mode A0 shows the least sensitivity to those of the other two modes, and Mode S0 at the lower frequency shows a greater sensitivity to that at the higher frequency (see Figure 9b and e).

Likewise, when the deformation under loading is ignored and only the thickness variation is considered, the values of phase and group velocity of GW in the plate under loading can be converted back to obtain the velocity differences as shown in Figure 10, whose correctness is validated via comparison of the result in Ref. [35]. This situation applies to the measurement with the excitation and acquisition bonded or integrated with the plate, in which the relative distance between excitation and acquisition may change under loading.

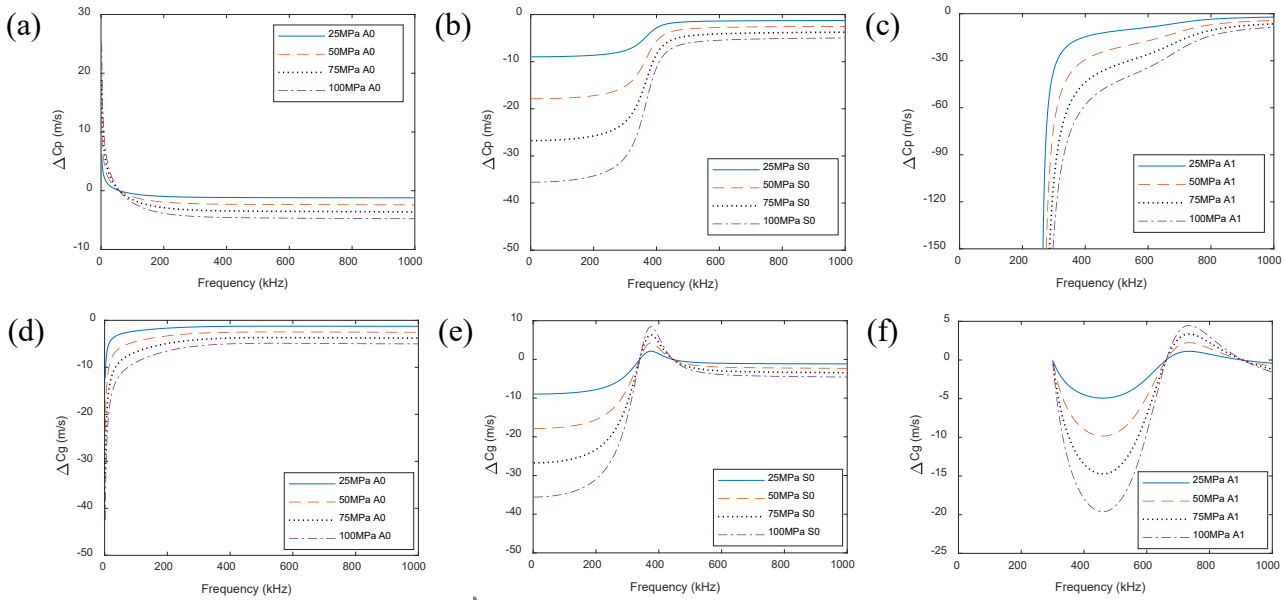

Figure 9 Phase (c_p) and group (c_g) velocity difference of GW along a 4 mm thick aluminum plate at different pre-stresses considering the deformation: (a) Δc_p – A0, (b) Δc_p – S0, (c) Δc_p – A1, (d) Δc_g – A0, (e) Δc_g - S0, and (f) Δc_g – A1.

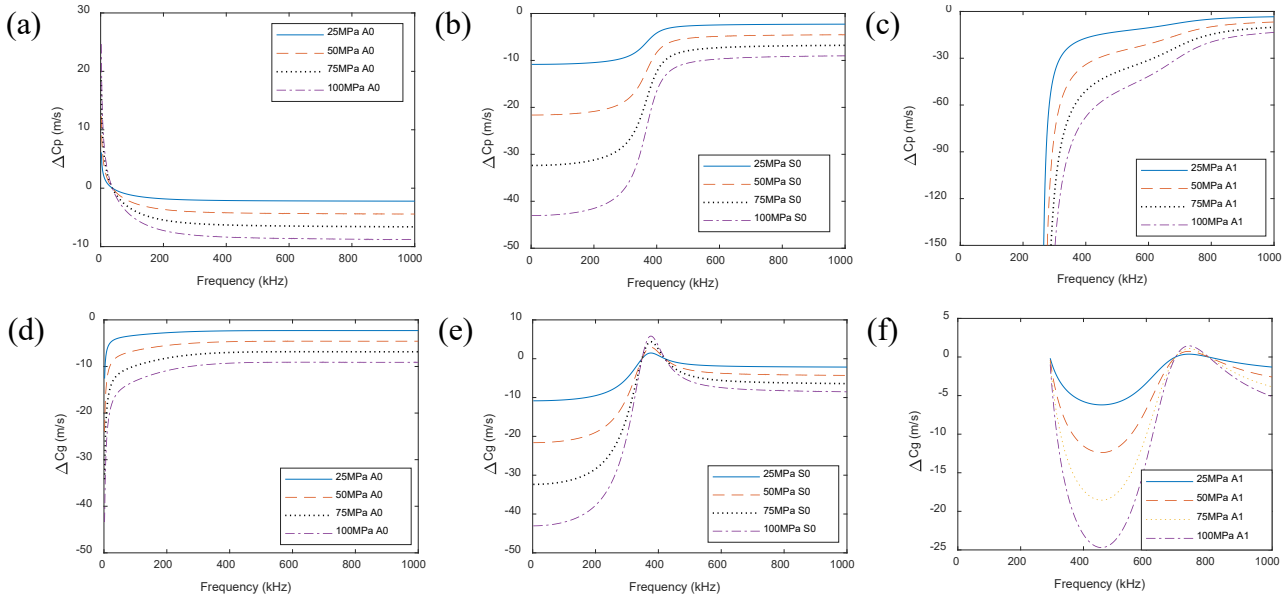

Figure 10 Phase (c_p) and group (c_g) velocity difference of GW along a 4 mm thick aluminum plate at different pre-stresses ignoring the deformation: (a) Δc_p – A0, (b) Δc_p – S0, (c) Δc_p – A1, (d) Δc_g – A0, (e) Δc_g - S0, and (f) Δc_g – A1.

4.3 **Anisotropic Plate - CFRP Laminate**

Without loss of generality, the GW propagating along 30^0 in a CFRP laminate made of AS4M3502 with the stacking sequence $[0/90/-45/45]_{2s}$ and a total thickness of 2 mm is investigated. The material properties of AS4M3502 are listed in Table 1, and the consumed computation time for single core and multiple cores is 109.05 s and 23.32 s, respectively, as listed in Table 2. The computed dispersion curves from 1D-GLL-SAFE in Figure 11a to c show a correct sorting of each mode and a good agreement with the

results computed from DC in Figure 11d to e. The calculated errors of phase velocity (see Figure 11g) and wave number (see Figure 11i) for the Modes A0, SH0, and S0 all reach below 1×10^{-4}, and that of the group velocity (see Figure 11h) can also reach below 3×10^{-2}, confirming the correctness of the developed algorithm. Note that although the GW modes can still be approximately classified as symmetric, anti-symmetric, and shear horizontal modes in the investigated laminate with symmetric and quasi-isotropic stacking sequence, this classification rule does not hold for laminate with arbitrary stacking sequence. Hence, only numeral numbering is adopted to name all the GW modes. Figure 12 shows the typical mode shapes of displacement for Mode 1 and Mode 3 in the plane consisting of the propagation and out-of-plane directions, together with the through-thickness profiles of the displacement components as shown in Figure 13. The displacement profiles show a complex pattern due to the different stacking sequences in each ply, and show an approximate anti-symmetric and symmetric pattern for Mode 1 and Mode 3 respectively due to the quasi-isotropic and symmetric stacking sequences for the investigated laminate. Furthermore, the stress and strain profiles along the thickness for Mode 1 at ~1000 kHz are shown in Figure 14, where the stress shows a much more significant discontinuity than the strain due to the change in material parameter from different stacking angles.

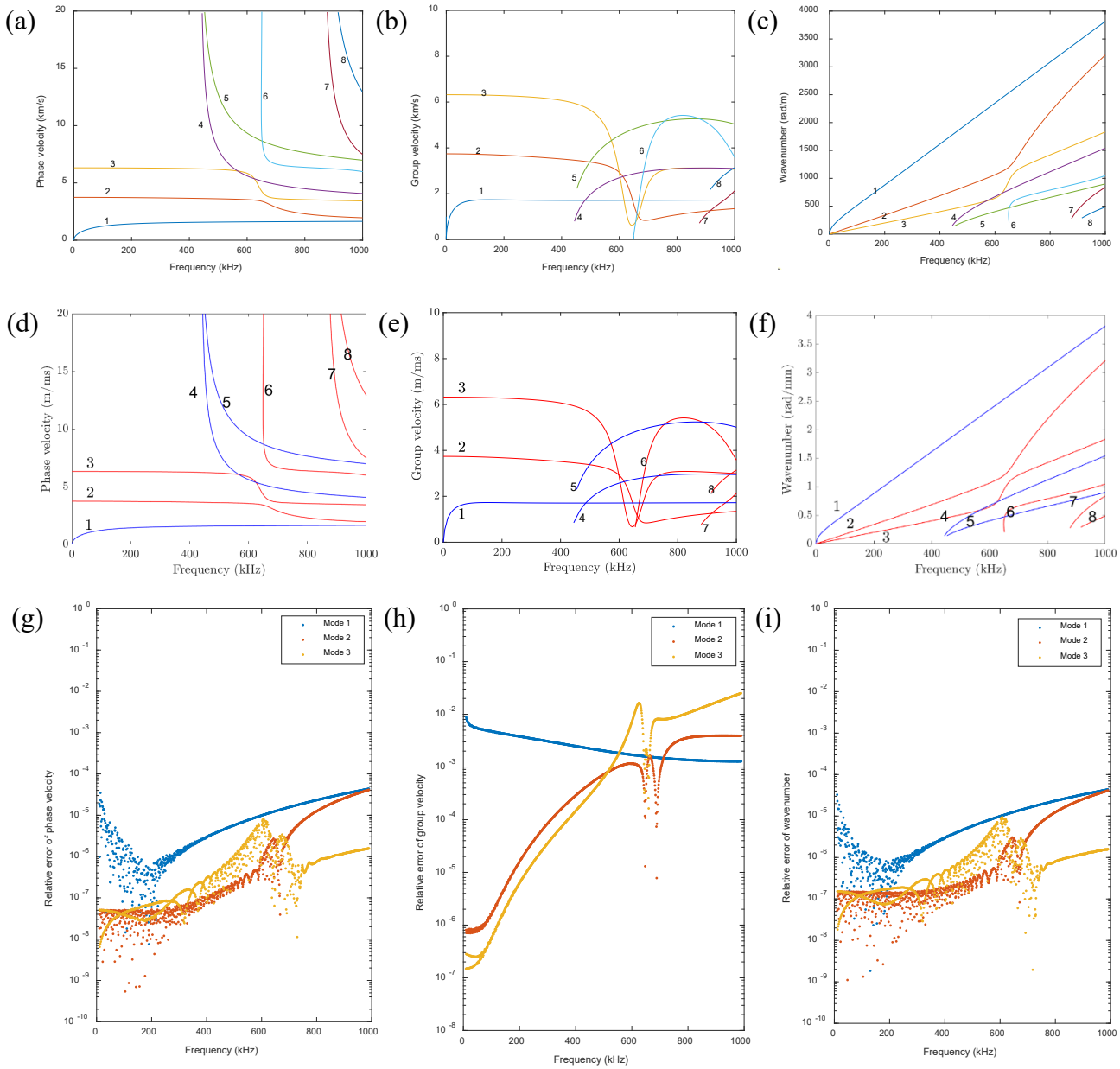

Figure 11 Dispersion curves of GW along 30^0 of AS4M3502 laminate $[0/90/-45/45]_{2s}$: (a) phase velocity from SAFEDC, (b) group velocity from SAFEDC, (c) wave number from SAFEDC, (d) phase velocity from DC, (e) group velocity from DC, (f) wave number from DC, (g) relative error of phase velocity, (h) relative error of group velocity, and (i) relative error of wave number.

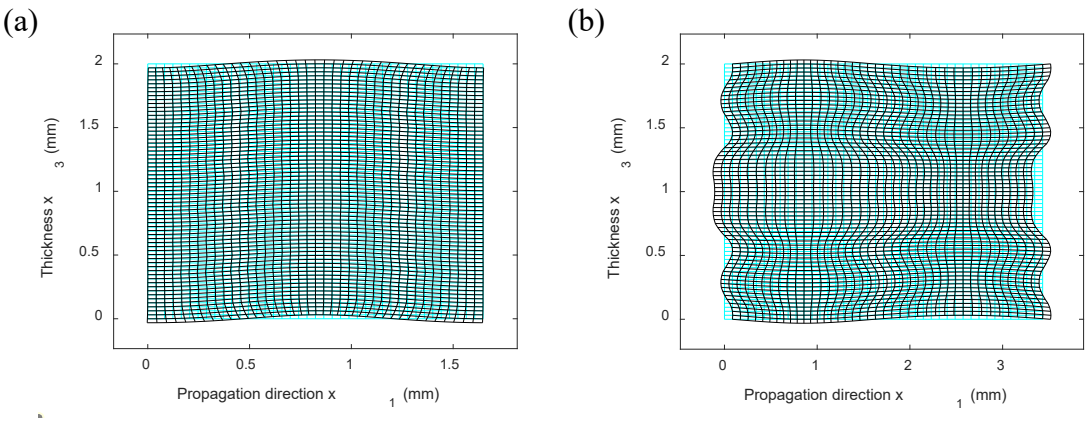

Figure 12 Mode shape of displacement superposed with undistorted shape for GW along 30^0 of

AS4M3502 laminate $[0/90/-45/45]_{2s}$ at ~1000 kHz: (a) Mode 1, (b) Mode 3

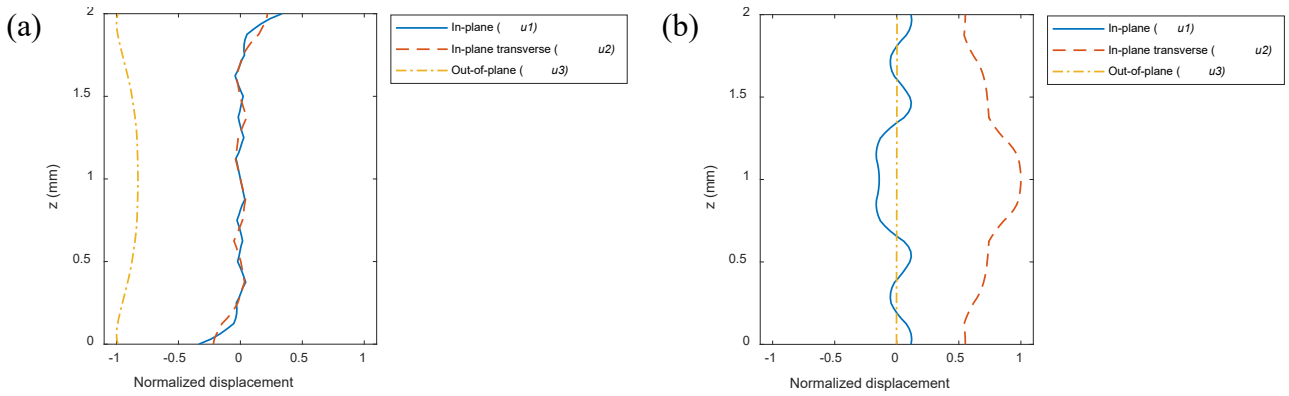

Figure 13 Profile of displacement of GW along 30^0 of AS4M3502 laminate $[0/90/-45/45]_{2s}$ at ~1000 kHz: (a) Mode 1, (b) Mode 3

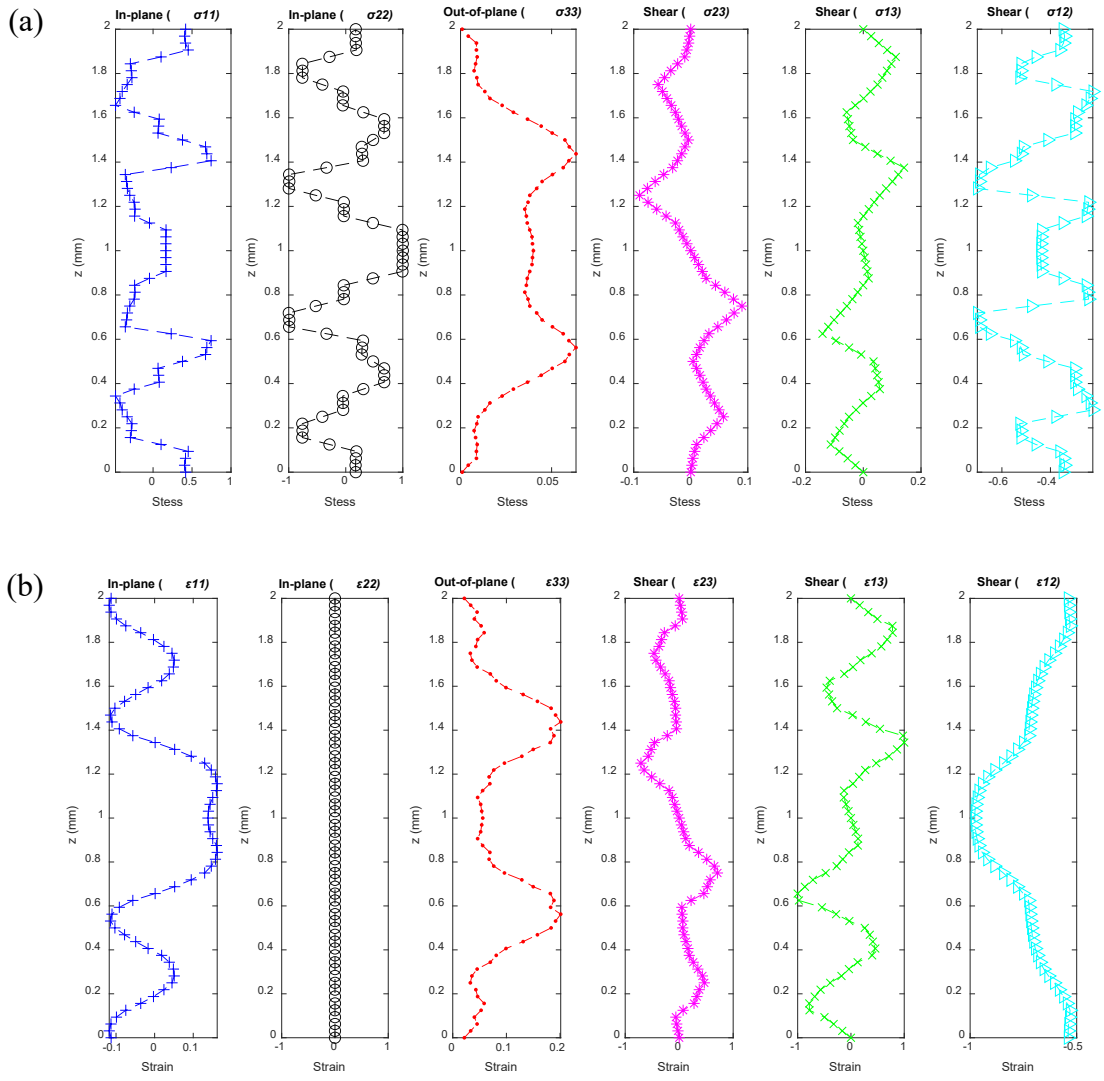

Figure 14 Mode 3 profile for GW along 30^0 of AS4M3502 laminate $[0/90/-45/45]_{2s}$ at ~1000 kHz: (a) stress and (b) strain along the thickness direction

4.4 General section – rail track

A typical rail track (80-lb. A.S.C.E.) made of steel alloy 1020 is selected to illustrate the 2D-Gauss-

SAFE computation of the GW propagating along the general section. With the maximum and minimum size of the triangular element entered as 5 mm and 4 mm, respectively, the discretized rail track with triangular elements is displayed in Figure 2. The element size can be freely varied in the developed tool SAFEDC, but it should be noted that extremely dense meshing should be avoided for two reasons: (1) rapidly increasing time and memory consumption and (2) usually lower order GW modes are concerned, whose computation with high accuracy can be easily achieved with relatively coarse meshing. With the wave number step set to 2 rad/m, the obtained group velocity dispersion curves (see Figure 15b) show a stronger discontinuity than the phase velocity (see Figure 15a) and wave number curves (see Figure 15c), as the group velocity is related to the derivative of the angular frequency to the wave number. In addition, incorrect mode sorting occurs, as a result of a large gap in the wave number. To correct these errors, the wave number step is reduced to 0.5 rad/m, and the resulting group velocity dispersion curve (see Figure 15e) is greatly improved in terms of mode sorting and curve smoothness. For the phase velocity and wave number dispersion curves (see Figure 15d and f), only a slight improvement can be carefully observed by increasing the number of computation points. With $\Delta\kappa = 0.5\,\mathrm{rad/m}$, The consumed computation time for single core and multiple cores is 83.16 s and 27.69 s, respectively, as listed in Table 2. Although the computation time at each wave number increases largely attributed to the increased element number for the general section compared with the plate structures, the setup of a lower maximum frequency (e.g. 30 kHz for the rail track) results in the total computation time for the general section usually on the same order or only one order larger than that for the plate structures. Overall speaking, the entire computation time is jointly decided by material, mesh, frequency, and wave number.

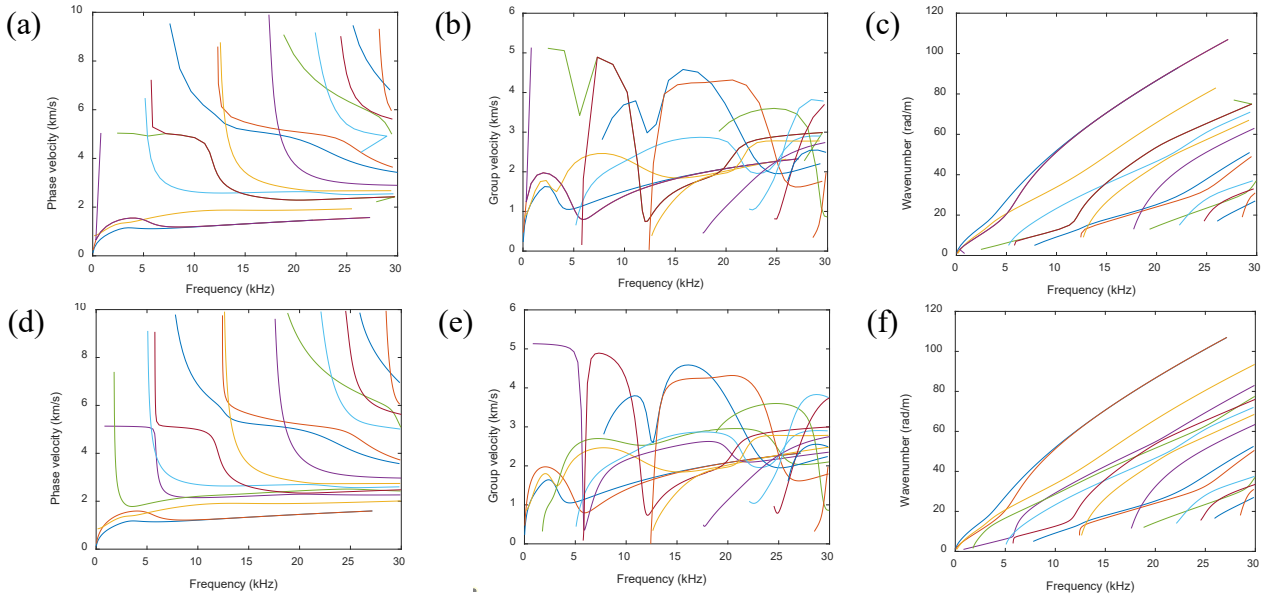

Figure 15 Dispersion curves of GW along a typical railway track: (a) phase velocity – frequency at $\Delta k = 2$ rad/m, (b) group velocity – frequency $\Delta k = 2$ rad/m, (c) wave number – frequency $\Delta k = 2$ rad/m, (d) phase velocity – frequency at $\Delta k = 0.5$ rad/m, (e) group velocity – frequency $\Delta k = 0.5$ rad/m, and (f) wave number – frequency $\Delta k = 0.5$ rad/m

In addition to the dispersion curves, users can also output the 2D contours of three normalized displacement components, as shown for Mode 1 at ~30 kHz in Figure 16a and Mode 3 at ~30 kHz in Figure 16b. It can be seen that for Mode 1, the displacement along the z-direction is much larger than those along the x- and y-directions. In addition, the displacement at the foot of the rail track has a larger amplitude than that at other positions. Therefore, Mode 1 at 30 kHz is suitable for detecting defects at the foot of the rail track, while being insensitive to defects at the head and web. Mode 3 at ~30 kHz, on the other hand, has a much larger amplitude at the web than that at the other positions, and is therefore suitable for web defect detection. SAFEDC also offers the 3D animation of the displacement for the single cross section or the 3D solid, as shown in Figure 16c to Figure 16e, which vividly illustrates the wave propagation.

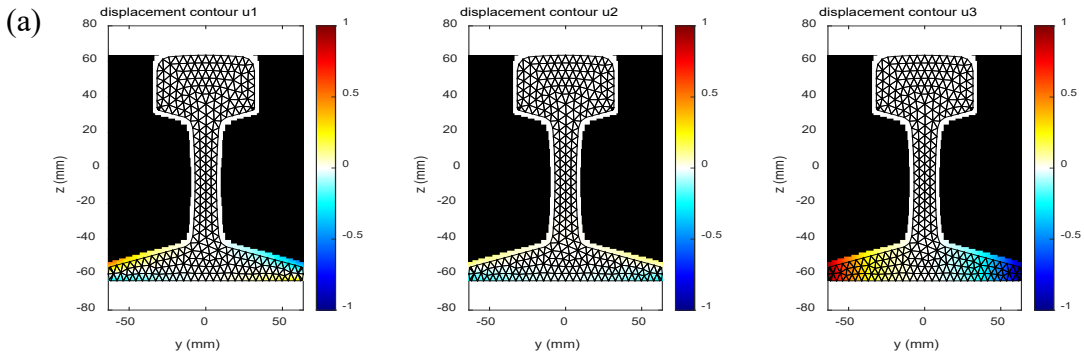

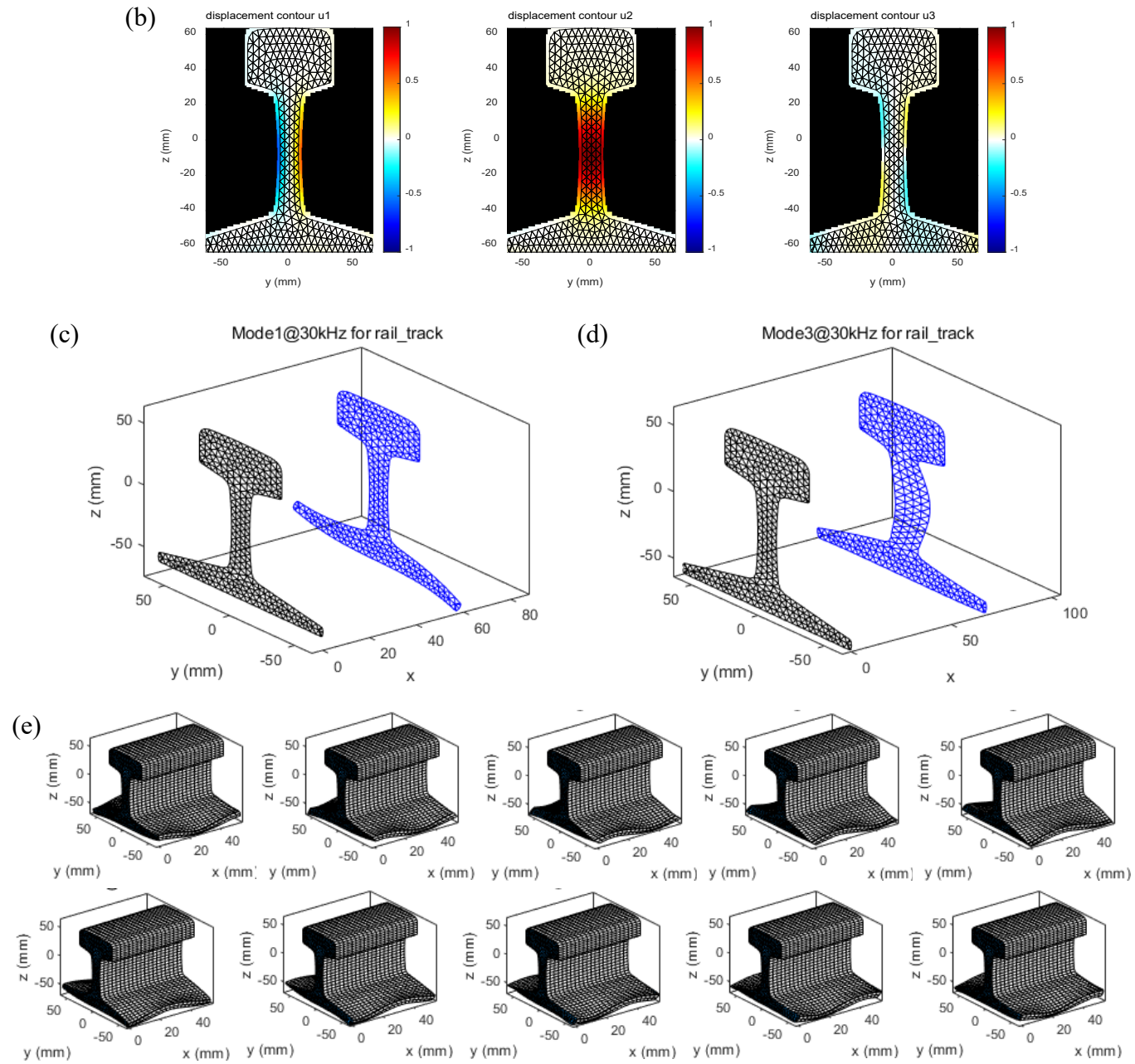

Figure 16 (a) 2D contour of displacement for Mode 1 at ~30 kHz, (b) 2D contour of displacement for Mode 3 at ~30 kHz, (c) mode shape of displacement for mode 1 at ~30 kHz, (d) mode shape of displacement for Mode 3 at ~30 kHz, and (e) snapshot of 3D displacement animation in a cycle with a time increment of 1/10 time period for Mode 1 at ~30 kHz.

5. Concluding Remarks

This study combines the 1D-GLL-SAFE algorithm for computing GWs in plate structures and the 2D-Gauss-SAFE algorithm for computing GWs in waveguides with complex geometry, and further develops the open-source tool SAFEDC, which is able to compute GWs in various waveguides with acoustoelasticity and material anisotropy.

The influence of acoustoelasticity on GW based on two different sets of governing equations is

compared in this study, which shows highly consistent results in terms of the phase velocity. In addition, to ease the complexity of the induced 4^{th} order tensor of EECs in the governing equation, the conversion from the 4^{th} order tensor to the Voight notation with split EECs is also validated, which shows the split EECs may lead to a slightly larger error under unidirectional loading. To avoid the ambiguity induced by the splitting of EECs, only the full 4^{th} order EEC tensor derived with the governing equation described by the initial coordinate system is adopted in SAFEDC to compute GW with acoustoelasticity.

The output of rich GW characteristics in SAFEDC will help the researchers and engineers to understand how GWs propagate in various waveguides and to select the appropriate GW for their specific research and application. For example, selecting the appropriate GW in the pipeline is essential for effective corrosion detection. For the stress characterization in isotropic plate structures, the analysis of GWs under different loading conditions is essential to select the GW mode and frequency that is most sensitive to stress.

In the near future, both the 1D-GLL-SAFE and 2D-Gauss-SAFE algorithms will be further developed and the results will be integrated into the open-source SAFEDC to provide more functionality, including

(1) Computation of GW in viscoelastic material. Viscoelastic material is easily added into SAFE with a search for eigenvalues of the wave number at a fixed frequency.

(2) Computation of GW in a waveguide immersed in a solid/fluid. Using the perfectly matched layer, SAFE is able to compute the GW in a general waveguide immersed in a solid/fluid.

(3) Interaction of GW with disbond/delamination. By combining all the calculated GW modes and the normal mode expansion method[8], the interaction of GW with disbond/delamination will also be investigated in the near future.

Declaration of competing interest

The authors declare that they have no known competing financial interests or personal relationships that could have appeared to influence the work reported in this paper.

Acknowledgement

The authors would like to thank the support from the National Natural Science Foundation of China (Grant Nos. 52105142, and 52205170), Basic and Applied Basic Research Foundation of Guangdong

Province (Grant No. 2023A1515011032), Shenzhen Stable Support Grant (Grant No. GXWD20201230155427003-20200731161831019), and Xiamen Natural Science Foundation (Grant No. 3502Z20227017).

Data availability

The freeware SAFEDC, together with the installation and usage guide, is available at https://sourceforge.net/projects/safedc/.

Appendix A.

Some typical interfaces of the freeware SAFEDC are shown below. The typical interface of the tab "Material editor" for the adopted isotropic aluminum alloy 6061 in Section 4.1 and AS4M3502 in Section 4.3 is shown in Figure A 1. The typical interface of the tab "Isotropic plate" for the adopted 4 mm thick isotropic aluminum alloy 6061 is shown in Figure A 2. The default interface of the tab "Anisotropic plate" is shown in Figure A 3, together with the setup of material AS4M3502 with the stacking sequence $[0/90/-45/45]_{2s}$ shown in Figure A 4. The default interface of the tab "General section" is shown in Figure A 5. The default interface of the tab "Advanced parameters" is displayed in Figure A 6.

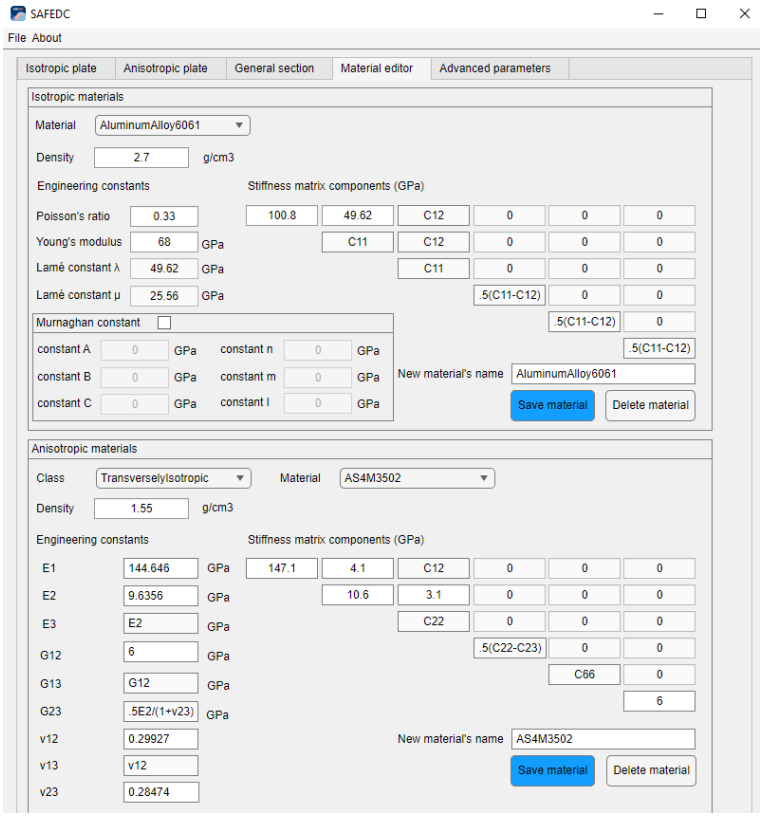

Figure A 1. Typical interface of the tab “Material editor”

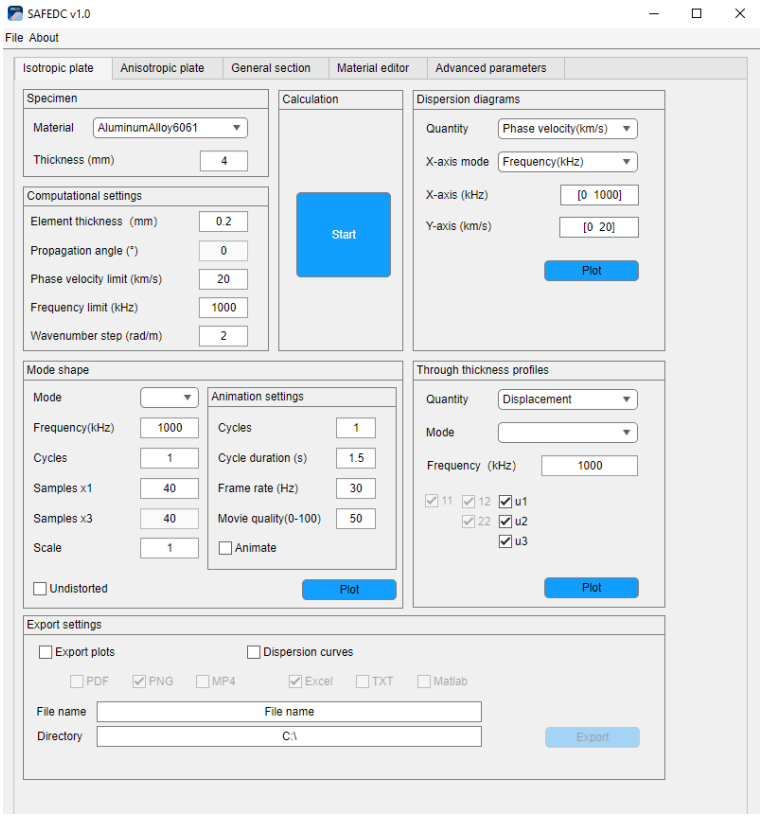

Figure A 2. Typical interface of the tab “Isotropic plate”

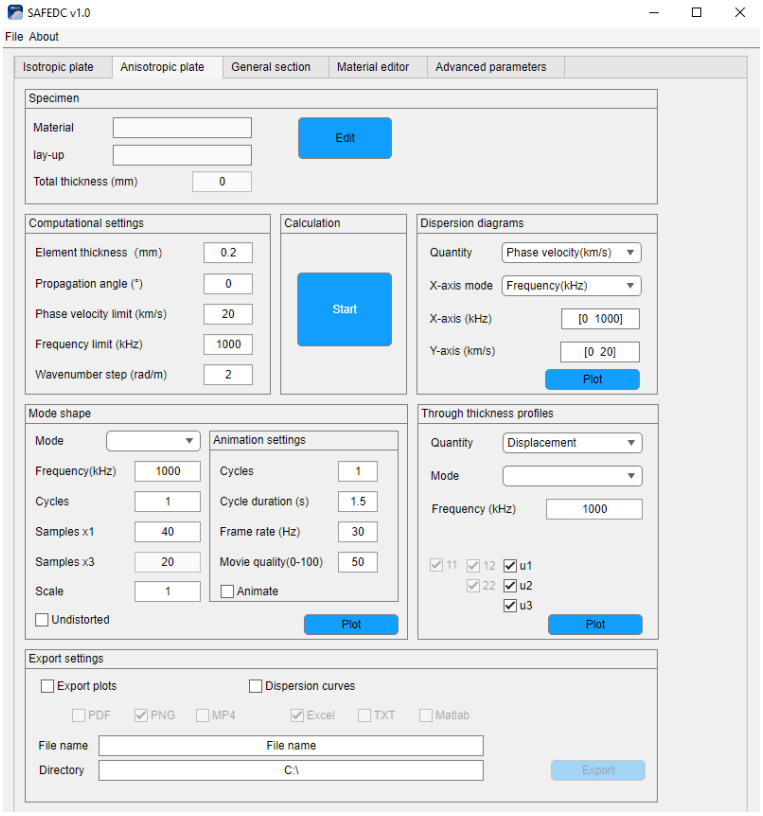

Figure A 3. Default interface of the tab “Anisotropic plate”

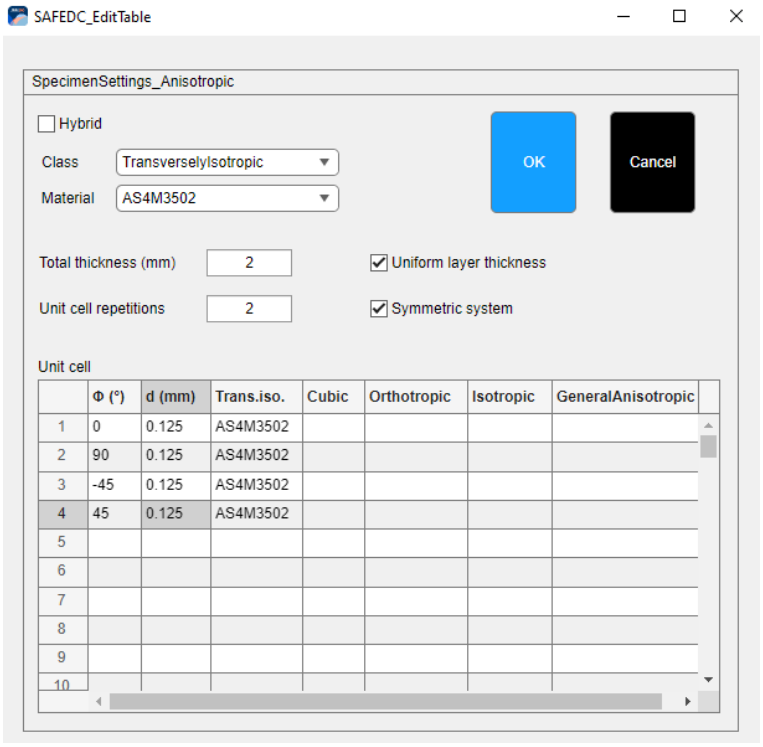

Figure A 4. Typical interface of material and geometry setup for anisotropic laminate

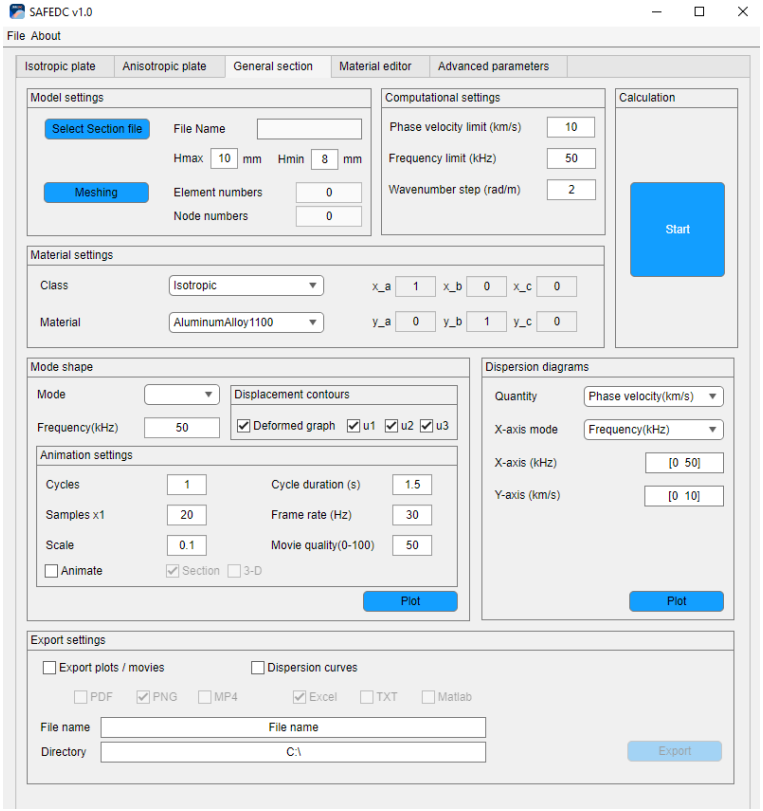

Figure A 5. Default interface of the tab “General section”

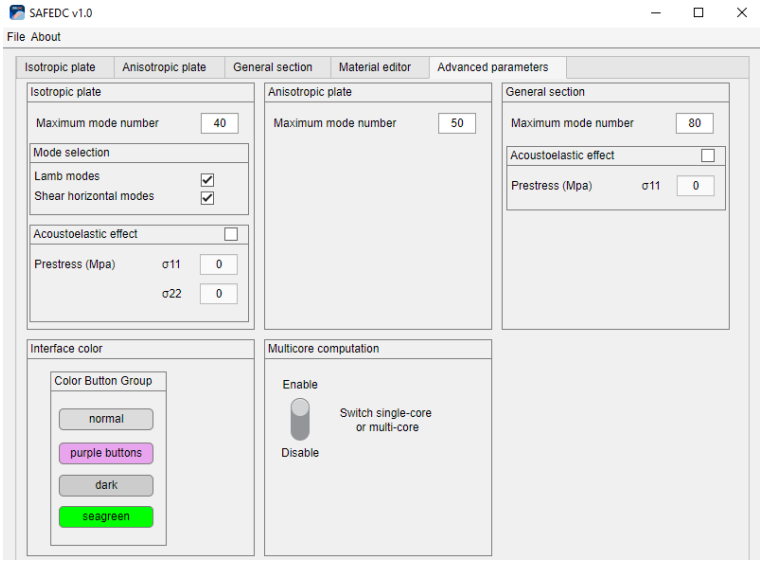

Figure A 6. Default interface of the tab “Advanced parameters”

Appendix B.

For isotropic material, the group velocity can be simply computed as:

$$c_g = \frac{\partial \omega}{\partial k} = \frac{\mathbf{Q}_L (i\mathbf{K}_2 + 2k\mathbf{K}_3)\mathbf{Q}_R}{2\omega \mathbf{Q}_L \mathbf{M} \mathbf{Q}_R}, \tag{B1}$$

where $\mathbf{Q}_L$ and $\mathbf{Q}_R$ are the left and right eigenvectors, respectively.

For anisotropic plates, the group velocity $\mathbf{c}_g$ has a radial component in the direction of k and an

angular component perpendicular to k. Thus the two group velocity components in a Cartesian coordinate with the wave vector along the angle θ can be obtained as:

$$\begin{Bmatrix} c_{gx} \\ c_{gy} \end{Bmatrix} = \begin{bmatrix} \cos\theta & -\sin\theta \\ \sin\theta & \cos\theta \end{bmatrix} \begin{Bmatrix} \dfrac{\partial\omega}{\partial k} \\ \dfrac{\partial\omega}{k\partial\theta} \end{Bmatrix}, \tag{B2}$$

where the derivative term $\partial\omega/\partial\theta$ can be approximated by the finite central difference:

$$\left.\frac{\partial\omega}{\partial\theta}\right|_{\theta=\theta_1} \approx \frac{\omega(k)\big|_{\theta_1+\Delta\theta/2} - \omega(k)\big|_{\theta_1-\Delta\theta/2}}{\Delta\theta} \tag{B3}$$

Therefore, the group velocity and direction in the anisotropic plate are:

$$\begin{cases} c_g = \sqrt{c_{gx}^2 + c_{gy}^2} \\ \theta_g = \arctan(\dfrac{c_{gy}}{c_{gx}}) \end{cases} \tag{B4}$$

References

[1] L. Qiu, X. Lin, Y. Wang, S. Yuan, W. Shi, A mechatronic smart skin of flight vehicle structures for impact monitoring of light weight and low-power consumption, Mech. Syst. Signal Process. 144 (2020) 106829. https://doi.org/10.1016/j.ymssp.2020.106829.

[2] X. Yu, P. Zuo, J. Xiao, Z. Fan, Detection of damage in welded joints using high order feature guided ultrasonic waves, Mech. Syst. Signal Process. 126 (2019) 176–192. https://doi.org/10.1016/j.ymssp.2019.02.026.

[3] M. V. Golub, O. V. Doroshenko, M.A. Arsenov, A.A. Eremin, Y. Gu, I.A. Bareiko, Improved Unsupervised Learning Method for Material-Properties Identification Based on Mode Separation of Ultrasonic Guided Waves, Computation. 10 (2022). https://doi.org/10.3390/computation10060093.

[4] Y. Hu, F. Cui, F. Li, X. Tu, L. Zeng, Sparse wavenumber analysis of guided wave based on hybrid Lasso regression in composite laminates, Struct. Heal. Monit. 21 (2022) 1367–1378. https://doi.org/10.1177/14759217211032118.

[5] Guided Wave Testing, (2023). https://www.applus.com/us/en/what-we-do/sub-service-sheet/guided-wave-ultrasonic-testing.

[6] SONYKS guided wave testing, (2023). https://www.eddyfi.com/en/product/sonyks-guided-waves-pipeline-inspection.

[7] GUL Subsea Solutions, (2023). https://www.guided-ultrasonics.com/gul-subsea-solutions/.

[8] K. Wang, M. Liu, W. Cao, W. Yang, Z. Su, F. Cui, Detection and sizing of disbond in multilayer bonded structure using modally selective guided wave, Struct. Heal. Monit. 20 (2021)

904–916. https://doi.org/10.1177/1475921719866274.

[9] Z. Su, L. Ye, Y. Lu, Guided Lamb waves for identification of damage in composite structures: A review, J. Sound Vib. 295 (2006) 753–780. https://doi.org/10.1016/j.jsv.2006.01.020.

[10] T. Druet, B. Chapuis, M. Jules, G. Laffont, E. Moulin, Passive SHM system for corrosion detection by guided wave tomography, in: Sensors, Algorithms Appl. Struct. Heal. Monit. IIW Semin. SHM, 2015, 2018: pp. 21–29.

[11] A. Abderahmane, A. Lhémery, L. Daniel, Stress imaging by guided wave tomography based on analytical acoustoelastic model, J. Acoust. Soc. Am. 151 (2022) 2863–2876. https://doi.org/10.1121/10.0010359.

[12] H.T. Hoang, T. Druet, B. Chapuis, E. Moulin, Passive tomography by elastic guided wave for corrosion detection in pipelines, in: IWSHM 2019 - 12th Int. Work. Struct. Heal. Monit., Stanford, 2019. https://doi.org/10.12783/shm2019/32189.

[13] M. Liu, Z. Li, S. Wang, Z. Zhang, C.M. Leung, Quantitative characterization of out-of-plane fiber wrinkling in thick CFRP with Double-side inverse-variance weight-synthetic ultrasonic imaging, Compos. Part A Appl. Sci. Manuf. 166 (2023) 107376. https://doi.org/10.1016/j.compositesa.2022.107376.

[14] Z. Zhang, S. Guo, Q. Li, F. Cui, A. Alexander, Z. Su, M. Liu, Ultrasonic detection and characterization of delamination and rich resin in thick composites with waviness, Compos. Sci. Technol. 189 (2020) 108016. https://doi.org/10.1016/j.compscitech.2020.108016.

[15] H. Lamb, P.R.S.L. A, On waves in an elastic plate, Proc. R. Soc. London. Ser. A, Contain. Pap. a Math. Phys. Character. 93 (1917) 114–128. https://doi.org/10.1098/rspa.1917.0008.

[16] M.J.S. Lowe, Matrix Techniques for Modeling Ultrasonic-Waves in Multilayered Media,

Ieee Trans. Ultrason. Ferroelectr. Freq. Control. 42 (1995) 525–542. https://doi.org/10.1109/58.393096.

[17] N. Gandhi, J.E. Michaels, S.J. Lee, Acoustoelastic Lamb wave propagation in biaxially stressed plates, J. Acoust. Soc. Am. 132 (2012) 1284–1293. https://doi.org/10.1121/1.4740491.

[18] F. Shi, J.E. Michaels, S.J. Lee, In situ estimation of applied biaxial loads with Lamb waves , J. Acoust. Soc. Am. 133 (2013) 677–687. https://doi.org/10.1121/1.4773867.

[19] A. Abderahmane, A. Lhémery, L. Daniel, Effects of multiaxial pre-stress on Lamb and shear horizontal guided waves, J. Acoust. Soc. Am. 149 (2021) 1724–1736. https://doi.org/10.1121/10.0003630.

[20] Z. Yang, K. Liu, K. Zhou, Y. Liang, J. Zhang, Y. Zheng, D. Gao, S. Ma, Z. Wu, Investigation of thermo-acoustoelastic guided waves by semi-analytical finite element method, Ultrasonics. 106 (2020) 106141. https://doi.org/10.1016/j.ultras.2020.106141.

[21] P. Zuo, X. Yu, Z. Fan, Acoustoelastic guided waves in waveguides with arbitrary prestress, J. Sound Vib. 469 (2020) 115113. https://doi.org/10.1016/j.jsv.2019.115113.

[22] Disperse, (2023). https://www.imperial.ac.uk/non-destructive-evaluation/products-and-services/disperse/.

[23] N. Gandhi, Determination of dispersion curves for acoustoelastic lamb wave propagation, Georgia Institute of Technology, 2010.

[24] P.W. Loveday, Semi-analytical finite element analysis of elastic waveguides subjected to axial loads, Ultrasonics. 49 (2009) 298–300. https://doi.org/10.1016/j.ultras.2008.10.018.

[25] T. Hayashi, W.J. Song, J.L. Rose, Guided wave dispersion curves for a bar with an arbitrary cross-section, a rod and rail example, Ultrasonics. 41 (2003) 175–183.

https://doi.org/10.1016/S0041-624X(03)00097-0.

[26] F. Seyfaddini, H. Nguyen-Xuan, V.H. Nguyen, A semi-analytical isogeometric analysis for wave dispersion in functionally graded plates immersed in fluids, Acta Mech. 232 (2021) 15–32. https://doi.org/10.1007/s00707-020-02818-0.

[27] A.M.A. Huber, The Dispersion Calculator: A free software for calculating dispersion curves of guided waves in multilayered composites, (2022). https://www.dlr.de/zlp/en/desktopdefault.aspx/tabid-14332/24874_read-61142/ (accessed June 17, 2022).

[28] P. Bocchini, A. Marzani, E. Viola, Graphical User Interface for Guided Acoustic Waves, J. Comput. Civ. Eng. 25 (2010) 202–210. https://doi.org/10.1061/(asce)cp.1943-5487.0000081.

[29] V. Giurgiutiu, LAMSS-COMPOSITES, (n.d.). http://www.me.sc.edu/Research/lamss/html/software.html.

[30] M. Liu, L. Li, Y. Zhang, G. Chen, F. Cui, Dispersion of guided waves in complex waveguides: a hybrid modeling technique combining gauss-lobatto-legendre node collation and semi-analytical finite element method, Int. J. Appl. Mech. (2022). https://doi.org/10.1142/S1758825122500855.

[31] P.W. Loveday, Simulation of Piezoelectric Excitation of Guided Waves Using Waveguide Finite Elements, IEEE Trans. Ultrason. Ferroelectr. Freq. Control. 55 (2008) 2038–2045.

[32] S. Eldevik, Measurement of non-linear acoustoelastic effect in steel using acoustic resonance, (2014) 272.

[33] D.D. Muir, One-Sided Ultrasonic Determination of Third Order Elastic Constants using

Angle-Beam Acoustoelasticity Measurements, Techniques. (2009).

[34] M. Liu, K. Wang, C.J. Lissenden, Q. Wang, Q. Zhang, R. Long, Z. Su, F. Cui, Characterizing hypervelocity impact (HVI)-induced pitting damage using active guided ultrasonic waves: From linear to nonlinear, Materials (Basel). 10 (2017). https://doi.org/10.3390/ma10050547.

[35] M. Mohabuth, A. Kotousov, C.T. Ng, Effect of uniaxial stress on the propagation of higher-order Lamb wave modes, Int. J. Non. Linear. Mech. 86 (2016) 104–111. https://doi.org/10.1016/j.ijnonlinmec.2016.08.006.